Initial Stage of Transition Process by Modal-Spectral Element Method

Jeyatharsan Selvanayagam

A Thesis

in

The Department

of

Mechanical and Industrial Engineering

Presented in Partial Fulfillment of the Requirements

for the Degree of Master of Applied Science (Mechanical Engineering) at

Concordia University

Montreal, Quebec, Canada

November 2009

Your file Votre référence
ISBN: 978-0-494-67214-3
Our file Notre référence
ISBN: 978-0-494-67214-3

Abstract

Initial Stage of Transition Process by Modal-Spectral Element Method

Jeyatharsan Selvanayagam

The initial stage of transition phenomena is investigated by numerically solving the complete Navier-Stokes equations for incompressible temporally evolving boundary layer flows on a flat plate. To force transition, the present investigation uses sufficiently small amplitude periodic perturbations at the inflow boundary and asymptotically decaying perturbation velocities and never-ending open boundary conditions at the far-field and outflow boundaries respectively. An initial steady state solution of the Navier-Stokes equation is assumed throughout the computational domain followed by the introduction of disturbances into the flow field. The reaction of this flow to such disturbances is studied by directly solving the Navier-Stokes equations using a highly accurate modal spectral element scheme developed by Niewiadomski [36]. The numerical scheme is recast to simulate our problem by incorporating various numerical algorithms. Furthermore, the computational results are discussed for a test case and several other simulation cases are considered to justify the initial stage of transition process. Finally, a demonstration of the suitability of the three dimensional aspect of the numerical method for the investigation of the temporal development of the two dimensional perturbations in the downstream locations is presented where the results are in fairly close agreement with the known numerical results of Fasel [05].

Acknowledgements

I would like to thank my supervising professor Dr. Marius Paraschivoiu for his continued intellectual guidance, encouragement and financial support throughout the course of this research. I would also like to express my deep gratitude to my parents and family members for their continued support and understanding.

Table of Contents

0.1 Nomenclature

Symbol:	Description
$u, v, w(\underline{u})$	velocity components (vector)
t	time
$\underline{f}$	body force
p	pressure
$\underline{\underline{\pi}}$	total stress tensor
$\underline{\underline{I}}$	identity tensor
$\underline{\underline{\tau}}$	extra stress tensor
ρ	fluid density
μ, υ	dynamic and kinematic viscosities
Re	Reynolds number
φ_{pqr}	basis functions
$\hat{u}_i$	vector of coefficients
v	trial function
η_1, η_2, η_3	collapsed coordinates
ξ_1, ξ_2, ξ_3	reference coordinates
x, y, z	physical Cartesian coordinates
h_j	Lagrange polynomial
P	expansion order
M	mass matrix
A	stiffness matrix
D	derivative matrix
C	convection operator
R_i	rotational matrix
U_∞	free-stream velocity
$\psi(x, y, t)$	stream function
A°	inflow amplitude factor
u'_A, v'_A	amplitude distributions from LST
u', v', w'	disturbance velocity components
U, V, W	mean flow velocity components
α	disturbance wave number
λ	wave length
β	disturbance frequency $(\beta = \beta_r + i\beta_i)$
β_r	oscillation frequency
β_i	amplification coefficient
c	wave velocity
δ_o^*	boundary layer displacement thickness at inflow
$\mathrm{Re}^\bullet$	Reynolds number based on displacement thickness

Chapter 1

Introduction

The main driving force of my research is the simulation of entire process of laminar-to-turbulent transition in a shear layer capturing transitional behavior accurately which is a basic scientific problem in modern fluid mechanics and has been the subject of study for over a century. The transition to turbulent flow has been simulated extensively with spectral and high order finite difference methods which provide higher accuracy solutions. However, the available standard CFD codes suffer from the inability to address this problem due to the requirements of higher order discretization and boundary and initial conditions. At the same time these methods are unable to handle complex geometries accurately. In order to model these complex geometries and to better suits for adaptability, higher order spectral element methods are employed which combines the geometric flexibility of finite element methods with the higher accuracy of spectral methods via tetrahedral elements. This spectral/hp element method was originally developed by Sherwin and Karniadakis [25],[50], where we can simultaneously increase the number of sub-domains (h-type refinement) and increase the interpolation order within the sub-domain (p-type refinement) either uniformly throughout the domain or selectively depending on the resolution requirements. Briefly, the spectral element method is summarized as, firstly decomposes the computational domain into sub-domains then obtains velocity and pressure representation through a summation of basis functions and corresponding coefficients, followed by the evaluation of mathematical

operations on the elemental level, which are then assembled to form global continuous expansion basis functions through a global assembly procedure.

The code, we used as a design tool to capture the geometry as well as the flow characteristics, was developed by Niewiadomski [36] in his PhD thesis. Herein this code was extended by incorporating new algorithms to simulate our problem. Through its increased accuracy as well as the use of GAMBIT generated structured or unstructured meshes, this code meets the requirements to simulate our problem in hand. Moreover, increased accuracy leads to more efficient use of computational resources and the higher order method requires less degree of freedom than the lower order methods to obtain the same accuracy.

1.1 Review of transitional flow

A computer program is used to study the initial stage of transition process in the boundary layer flow based on the spectral element scheme. A natural application for this analysis is the boundary layer behavior over an aero-plane wing. The boundary layer is the thin region of shear between the wing surface where the flow velocity vanishes due to adherence, and the free-stream where the flow can be considered as uniform, at the speed of the aero-plane. We have taken in the present analysis, a very thin wing without angle of attack, a flat plate.

The objective of the research is to implement incompressible Navier-Stokes equations by spectral element discretization to capture the initial stage of laminar-to-turbulent transition along a flat plate by applying appropriate boundary and initial conditions.

For the past century, numerous investigations have been conducted in an attempt to predict the transition process from laminar to turbulent flow in boundary layers which is a stability problem changing over time and space based on the idea that laminar flow is acted on by some small disturbances, this is still a challenging and fully unsolved problem. The transition process can be considered as six successive stages distinctly observable in physical experiments as shown by Stuart [54] in a review paper. According to Narasimha [34], natural transition is a multi-stage process involving linear evolution, secondary instability, break down and transition to turbulence. Following the stable laminar flow, the transition process starts out with the unstable two-dimensional Tollmien-Schlichting (T-S) waves and their amplification in the downstream direction is well described by primary (linear) stability theory. As these primary unstable waves exceed a critical threshold value, three dimensional waves and vortex structures evolve with alternating peaks and valleys result in a Λ-shaped vortical structure which is well treated by secondary stability theory. At the later stage, these three-dimensional vortex structure decays and form turbulent spots. Finally the sequences of these stages become fully turbulent flow. In other words, we can say that these are the preliminary stages to fully turbulent boundary layer flows [03].

Most of this effort stems from the early theoretical accomplishments of Orr [41],[42] and Sommerfeld [51]. Their achievement, based on linearized disturbance equations, is a successful example of classical hydrodynamic stability theory and is referred to as the Orr-Sommerfeld equation. As a first application, Tollmien [56],[57] investigated the stability of the boundary layer on a flat plate by solving the Orr-Sommerfeld equation, and this solution led to the calculation of a critical Reynolds number for the onset of

instability. This was convincingly demonstrated in the landmark experiments by Schubauer and Skramstad [47], who used a vibrating ribbon to trigger a disturbance into the boundary layer and phase velocity of the disturbance waves for comparing experimental measurements with theory. Gaster [10] has shown that, the use of the phase velocity for relating the temporal development of the theory with spatial development of the experiments was approximately correct. It was clearly shown that the disturbance development was in the downstream location, with amplitudes of the disturbances growing or decaying with increasing distance from the leading edge [47],[48]. This was repeated in a somewhat more refined manner by Ross et al [44]. As suggested by Gaster [11], in the linear stability theory a reformulation of the Orr-Sommerfeld equation for the case of space amplified disturbances and numerical solutions have enabled direct comparison of the results with theory and experimental measurements [20],[60]. With these and others contributions theory and experiments now agreed approximately on the initial growth of disturbances. From this Orr-Sommerfeld equation, much is now understood concerning boundary layer disturbances, more commonly referred to as the Tollmien-Schlichting waves. Since its origination, stability theory has gained wide acceptance and is now a well-established tool in research and engineering community. Nevertheless, qualitative and quantitative differences between the theory and experiments remained. The differences were attributed to the non-parallel effects which were excluded in the standard parallel theory [20] where it was argued that due to the slow growth of the boundary layer as the square root of the spatial distance x from the leading edge, the assumptions of a parallel base flow and of a disturbance amplitude distribution that was only dependent on the normal coordinate y (and not on the downstream coordinate x)

would be acceptable. Because of these assumptions the parallel theory did not fully agree with the experimental measurements in particular with respect to the growth rates and the critical Reynolds number. As a result, non-parallel effects resulting from the boundary layer growth in the downstream direction are considered which means that no restriction on the form of equation since the ensuring development of the perturbations is described by the complete Navier-Stokes equations and no linearization is necessary anywhere [07].

It is well demonstrated that the three dimensional disturbance environment is needed to observe the whole stages of transitional flow by many authors [27]. This three dimensional disturbance helps to keep the flow disturbance in growth and go to transition and turbulence for high Reynolds number. If there is only a two dimensional disturbance in the environment, then all we observe is the linear growth of the T-S waves in a certain range of Reynolds number, then the two dimensional disturbance dies down.

Following experimental and theoretical results, we can categorize transitions into two types for superimposed periodic oscillations: the harmonic K-type after Klebanoff [27] and the sub-harmonic H-type (H for Herbert [16],[17]) corresponding to the chosen amplitude of the initial disturbances. If the inflow perturbation is relatively high, K-type transition is expected which shows an aligned pattern. Contrast to the K-type transition, H-type needs low inflow perturbation which results staggered pattern in the transition region [03],[46].

In the present study we addressed the initial stage of transition process, namely the development of two dimensional Tollmien-Schlichting waves. These waves on a flat plate boundary layer are initiated in a disturbance environment with very small amplitudes. The development during this first stage, the so called T-S waves is well

described by the linear stability theory which predicts conditions whether the flow is stable or unstable to periodic disturbances. Therefore, the established boundary layer flow in the current work uses periodic disturbances of small amplitudes from the linear stability theory for inflow forcing which are constantly introduced into the flow field. The reaction of this flow (i.e. the temporal development of the perturbations) is then directly determined by the Navier-Stokes equations for incompressible flow which are solved using an accurate numerical procedure such as a spectral element method in a specified computational domain. The present work requires the calculation of the unsteady flow field that arises from the time-dependent perturbations. Therefore, the critical task is the application of initial and boundary conditions in the modal spectral element method that would yield a realistic resolution of the time dependent transitional flow character.

1.2 Thesis contribution

Important contributions are made toward the application of boundary and initial conditions in the modal spectral element method. At the inlet boundary, time periodic perturbation functions superimposed to the Blasius profiles are employed to impose disturbances into the flow field. The upper boundary condition is selected to overcome the erroneous due to the asymptotically decaying perturbation velocities in the far-field. Both of these inlet and far-field boundary conditions are chosen from Fasel [05]. Concerning the outflow boundary, many conditions can be applied such as linearized convective equation or Navier-Stokes equation without pressure gradient term [09] or stream-wise periodicity [52] or open boundary conditions [12] or buffer-domain technique [22],[31] etc. From these conditions, buffer domain technique has been used for the numerical simulation of flow transition by many researchers. This technique was

introduced by Streett [53] to treat the non-reflecting outflow boundary. Thus, a small portion of the downstream computational domain was appended to the end of the original outflow boundary to eliminate all possible convective wave reflections or upstream propagation of information which means that the waves exit the outflow boundary without wave reflection. The problem was, in general, that the conventional buffer domain was too long (usually four to eight T-S wavelengths) which greatly increases computational cost. Recently, this buffer domain length was brought up to a single T-S wavelength but still there exists undesirable cost [31],[22]. However, in this numerical study we used a passive open boundary condition (never-ending one) which works better than any other alternatives demonstrated by Gresho [12]. This condition is naturally included in the weak formulation of the Navier-Stokes equation in spectral element method. At the same time, this condition properly captures the flow physics. For the flat plate and both side walls in the span-wise directions, no-slip and arbitrarily slip boundary conditions are imposed respectively with no-penetration. Finally, due to the investigation of very small disturbances and by that the unwanted initial distortions of transient behaviors are eliminated by applying steady state solution of the Navier-Stokes equation rather than employing the Blasius solution as initial condition [05]. These employed boundary and initial conditions, allow us to observe temporal development of the perturbations in the downstream direction of the boundary layer.

1.3 Structure of the thesis

The thesis is organized as follows: The first chapter presents a brief introduction of the relevant studies of transitional process and the contribution in this dissertation. Chapter 2 introduces governing equations and reviews the spectral element method code developed

by Niewiadomski [36]. Chapter 3 focuses on the application of boundary and initial conditions in the spectral element method. This is followed by a validation procedure of the numerical method with Blasius solution for the suitability of the code to solve flat plate boundary layer flows. In Chapter 4, initial stage of transition phenomena is investigated by choosing appropriate boundary and initial conditions. To study this transitional behavior, small amplitude periodic disturbances are introduced into the flow field from the linear stability theory. Validation is performed by comparing the temporal development of the two dimensional disturbances at the down stream locations with the known results from Fasel [05]. Finally, Chapter 5 gives concluding remarks with suggestions of future work as well as suggestions for improvements to the code.

Chapter 2

Spectral Element Method

2.1 Governing Equations

Scalar differential equation for the mass balance is given by:

$$\frac{\partial \rho}{\partial t} + \nabla.(\rho \underline{u}) = 0 \tag{2-1}$$

which holds at every point in a flowing fluid. This equation is known as the continuity equation, and it expresses the physical law that mass is conserved.

Conservation of linear momentum in a flowing fluid is given by the following equation of motion:

$$\frac{\partial(\rho \underline{u})}{\partial t} = -\nabla.(\rho \underline{u}\underline{u}) - \nabla.\underline{\underline{\pi}} + \rho \underline{f} \tag{2-2}$$

This equation is valid for compressible and incompressible fluids of all types of Newtonian and non- Newtonian fluids. After simplifying the above equation of motion by continuity equation, we arrive at the following equation of motion for general fluids:

$$\rho\left(\frac{\partial \underline{u}}{\partial t} + \underline{u}.\nabla \underline{u}\right) = -\nabla.\underline{\underline{\pi}} + \rho \underline{f} \tag{2-3}$$

In the above equation, nature of the molecular forces is described by the total stress tensor $\underline{\underline{\pi}}$. There are two major contributions to the total stress tensor $\underline{\underline{\pi}}$: the thermodynamic pressure p and the deformation of the fluid $\underline{\underline{\tau}}$ called extra stress tensor. Thus, we can relate the total stress tensor as:

$$\underline{\underline{\pi}} = \underline{\underline{\tau}} + p\underline{\underline{I}} \tag{2-4}$$

An equation that specifies $\underline{\underline{\tau}}$ for a fluid is called stress constitutive equation which expresses the molecular stresses generated in the flow in terms of kinetic variables such as velocities and derivatives of velocities.

In this thesis, we considered the simplest constitutive equation for a Newtonian fluid. There are two versions for the Newtonian constitutive equation, one for compressible and a second for incompressible fluids. The Newtonian constitutive equation for compressible fluids is given by:

$$\underline{\underline{\tau}} = -\mu\left[\nabla\underline{u} + (\nabla\underline{u})^T\right] + \left(\tfrac{2}{3}\mu - k\right)(\nabla.\underline{u})\underline{\underline{I}} \tag{2-5}$$

where μ is the Newtonian shear viscosity and k is the bulk viscosity. The shear viscosity is the coefficient that describes the resistance of a fluid to sliding motion, and this is the primary material parameter which will be concerned in this thesis. For a fluid of constant density, that is, ρ is not a function of space or time, the equation of conservation of mass becomes as:

$$\nabla.\underline{u} = 0 \tag{2-6}$$

The above equation simplifies the compressible Newtonian constitutive equation to an incompressible Newtonian constitutive equation as:

$$\underline{\underline{\tau}} = -\mu\left[\nabla\underline{u} + (\nabla\underline{u})^T\right] \tag{2-7}$$

The equation of motion has a term $-\nabla.\underline{\underline{\pi}}$, which contains the unknown linear vector function $\underline{\underline{\pi}}$, the total stress tensor. Examining this term with the constitutive equation, we obtain:

$$-\nabla.\left(\underline{\underline{\tau}}+p\underline{\underline{I}}\right)=-\nabla p+\mu\nabla.\left[\nabla\underline{u}+\left(\nabla\underline{u}\right)^{T}\right] \tag{2-8}$$

The term $\mu\nabla.(\nabla\underline{u})^{T}$ simplified to $\mu\nabla(\nabla.\underline{u})$. The continuity equation is used to reduce this term to zero $(\nabla.\underline{u}=0)$ for incompressible fluids. Finally the equation of motion can be written as:

$$\rho\left(\frac{\partial\underline{u}}{\partial t}+\underline{u}.\nabla\underline{u}\right)=-\nabla p+\mu\nabla^{2}\underline{u}+\rho\underline{f} \tag{2-9}$$

This is the well known Navier- Stokes equation for an incompressible Newtonian fluid [33]. Derived conservation of mass (the continuity equation) and the conservation of momentum (the equation of motion) equations are non-dimensionalized by two scaling variables such as a characteristic length L and a characteristic velocity U. All variables in equations (2-6) and (2-9) are dimensional and are related to their dimensionless counter parts, denoted by bars, as follows:

$$\begin{gathered}\bar{x}=\frac{x}{L},\ \bar{y}=\frac{y}{L},\ \bar{z}=\frac{z}{L},\ \bar{u}=\frac{u}{U},\ \bar{v}=\frac{v}{U},\ \bar{w}=\frac{w}{U}\\ \bar{f}=\frac{fL}{U^{2}},\ \bar{t}=\frac{tU}{L},\ \bar{p}=\frac{p}{\rho U^{2}},\ \mathrm{Re}=\frac{\rho UL}{\mu}\end{gathered} \tag{2-10}$$

Thus, the dimensionless momentum equation becomes:

$$\frac{\partial\bar{\underline{u}}}{\partial t}+\bar{\underline{u}}.\nabla\bar{\underline{u}}=-\nabla\bar{p}+\frac{1}{\mathrm{Re}}\nabla^{2}\bar{\underline{u}}+\bar{\underline{f}} \tag{2-11}$$

The above non-dimensionalized momentum equation is solved along with the continuity equation and boundary conditions to compare differently scaled velocity field and other flow variables. From this point onward in our thesis, bars will not be indicated in all non dimensionalized equations.

2.2 Galerkin Method

To solve partial differential equations, there existed an approximation technique called the method of weighted residuals which replaces the infinite expansion of the exact solution by a finite expansion with an error term. In the spectral element method, an approximate solution is defined by the summation of all the bases over all elements with their respective coefficients:

$$u^{\delta} = \sum_{i=1}^{N_{dof}} \hat{u}_i \varphi_i \tag{2-12}$$

where $\varphi_i, \hat{u}_i$ are the basis functions and their respective coefficients correspondingly. Similarly, a trial function v is also formed. A weak formulation of the Navier-Stokes equation can be obtained by multiplying a trial function v with the Navier-Stokes equation ($E(u) = 0$) and integrating over the entire computational domain:

$$(v, E(u)) = \int_{\Omega} vE(u)\partial\Omega = 0 \tag{2-13}$$

By substituting the approximate solution into the Navier-Stokes equation, it results in a non-zero residual $E(u^{\delta}) = R(u^{\delta}) \neq 0$, which in the inner product becomes $(v, E(u^{\delta})) = (v, R(u^{\delta}))$. Unknown coefficients $\hat{u}_i$ and the residual $R(u^{\delta})$ make the set of algebraic equations unsolvable. To solve the above set of equations, the inner product of the residual $(v, R(u^{\delta}))$ is forced to zero by decreasing the element size or increasing the expansion order; thus, the solution approaches the exact solution. In the present work, we have considered the Galerkin method because the spectral element method is based on the Galerkin method where trial functions equal to the basis functions.

The Navier-Stokes equation ensures a divergence-free flow. Thus two different function spaces have to be defined, one for the velocity u and another for the pressure p. The function space for the velocity is defined as:

$$H_0^1(\Omega) = \left\{ v \in H^1(\Omega) \mid v = 0 \ \ on \ \ \partial\Omega \right\} \tag{2-14}$$

where H^1 requires that its members v as well as the gradients of the members ∇v are square integrable.

The function space for pressure is defined as:

$$L_0^2(\Omega) = \left\{ q \in L^2(\Omega) \mid \int_\Omega q \partial\Omega = 0 \right\} \tag{2-15}$$

where L_0^2 requires that its members are square integrable and its integral over the domain is zero. Thus the weak formulation of the Navier-Stokes equations for $u \in \left[H_0^1(\Omega)\right]^3$ and $p \in \left[L_0^2(\Omega)\right]$ are given by:

$$\left(v, \frac{\partial u}{\partial t}\right) + (v, u.\nabla u) = -(v, \nabla p) + \frac{1}{\mathrm{Re}}(v, \nabla^2 u) + (v, f) \qquad \forall v \in \left[H_0^1(\Omega)\right]^3 \tag{2-16}$$

Further simplification is performed through integration by parts, thus reducing the second derivative to a first derivative:

$$(v, \nabla^2 u) = \left[v \nabla u\right]_{\partial\Omega} - (\nabla v, \nabla u) \tag{2-17}$$

where [] denotes the evaluation at the boundary of the domain $\partial\Omega$. Note that the Neumann boundary condition is already set into the weak formulation as:

$$\left(v, \frac{\partial u}{\partial t}\right) + (v, u.\nabla u) + \frac{1}{\mathrm{Re}}(\nabla v, \nabla u) = -(v, \nabla p) + (v, f) \qquad \forall v \in \left[H_0^1(\Omega)\right]^3 \tag{2-18}$$

$$(\nabla.u, q) = 0 \qquad \forall q \in \left[L_0^2(\Omega)\right] \qquad (2\text{-}19)$$

where the brackets indicate an integral of the internal product over the domain. u, p, f are the velocity, pressure and forcing vectors while v and q are the test functions used for the velocity and pressure approximations.

2.3 Consistent Splitting Method

In order to design a highly accurate numerical scheme and to optimize any pressure errors, a consistent splitting scheme was introduced by Guermond [13]. The key idea behind this scheme is to evaluate the pressure by testing the momentum equation against gradients with extrapolation of pressure for the velocity calculation. By taking the L^2 inner product of the momentum equation in (2-16) with ∇q, and noticing that $(u_t, \nabla q) = -(\nabla.u_t, q) = 0$, we obtain:

$$\int_\Omega \nabla p \nabla q \partial\Omega = \int_\Omega \left(f - u.\nabla u + \frac{1}{\mathrm{Re}} \nabla^2 u\right) \nabla q \partial\Omega \quad \forall q \in H^1(\Omega) \qquad (2\text{-}20)$$

$$(\nabla p, \nabla q) = \left(f - (u.\nabla u)^* + \frac{1}{\mathrm{Re}} \nabla^2 u, \nabla q\right) \qquad (2\text{-}21)$$

We need two consecutive steps to find the velocity and pressure. First, we compute the velocity by making explicit the pressure in the weak formulation of momentum equation then we update the pressure by making use of (2-21). The accuracy of the above scheme can be improved by replacing the term $\nabla^2 u$ in (2-21) with the identity $\nabla^2 u = \nabla\nabla.u - \nabla \times \nabla \times u$. Due to the incompressibility constraint, $\nabla\nabla.u$ is zero, therefore the Laplacian term $\nabla^2 u$ is only reduced to a rotational term $-\nabla \times \nabla \times u$. Advantage of this formulation is that spurious pressure modes do not appear in the solution. The resulting fully discretized formulations are given by:

$$\left(v, \frac{Du^{k+1}}{\Delta t}\right) + \frac{1}{\mathrm{Re}}\left(\nabla v, \nabla u^{k+1}\right) = -\left(v, \nabla p^{*,k+1}\right) + \left(v, f(t^{k+1})\right) - \left(v, (u.\nabla u)^{*,k+1}\right) \tag{2-22}$$

$$\left(\nabla p^{k+1}, \nabla q\right) = \left(f^{k+1} - (u.\nabla u)^{*,k+1} - \frac{1}{\mathrm{Re}} \nabla \times \nabla \times u^{k+1}, \nabla q\right) \tag{2-23}$$

where $Du^{k+1} = \frac{3}{2}u^{k+1} - 2u^k + \frac{1}{2}u^{k-1}$ is an implicit approximation and $p^{*,k+1} = 2p^k - p^{k-1}$ and $(u.\nabla u)^{*,k+1} = \frac{8}{3}(u.\nabla u)^k - \frac{7}{3}(u.\nabla u)^{k-1} + \frac{2}{3}(u.\nabla u)^{k-2}$ are explicit approximations for the pressure and convection operator respectively.

2.4 Hierarchical Bases

In the spectral element method three coordinate systems are used. They are physical, reference and collapsed coordinate systems. The reference coordinate system is the barycentric coordinate system, defined in terms of volumes and the collapsed coordinate system is the transformation of a reference hexahedron onto a reference tetrahedron by the following three steps. Firstly, the hexahedron is reduced onto a prism by collapsing the top face of the hexahedron onto an edge. Secondly the prism is reduced to a square based pyramid by collapsing the top edge onto a vertex. Finally, the pyramid is reduced to a tetrahedron through the collapse of an edge on the base of the pyramid onto a vertex. The above three step transformation procedure is summarized by a single step transformation, which collapses a hexahedron onto a tetrahedron. The transformation from collapsed to reference coordinates is given by:

$$\xi_1 = \frac{(1+\eta_1)(1-\eta_2)(1-\eta_3)}{4} - 1$$

$$\xi_2 = \frac{(1+\eta_2)(1-\eta_3)}{2} - 1 \tag{2-24}$$

$$\xi_3 = \eta_3$$

where (ξ_1, ξ_2, ξ_3) and (η_1, η_2, η_3) are the reference and collapsed coordinate systems respectively. Inverse transformation of a tetrahedron onto a hexahedron is given by:

$$\eta_1 = \frac{4(1+\xi_1)}{(1-\xi_2)(1-\xi_3)} - 1$$

$$\eta_2 = \frac{2(1+\xi_2)}{(1-\xi_3)} - 1 \qquad (2\text{-}25)$$

$$\eta_3 = \xi_3$$

In the inverse operation, it is seen that this mapping is singular at the points $\xi_2 = 1$ and $\xi_3 = 1$, which are the vertices C and D respectively, although the coordinate values are not defined at these singularities. To prevent this problem different quadrature rules are used which do not include the values at these singularities. This will be discussed under the subsection of elemental operations.

Due to its orthogonality and rotational symmetry, the collapsed coordinate system is used to form the basis function in the spectral element method. The main criteria for designing basis functions are to ensure orthogonality of the Legendre inner product over each elemental region. The current three dimensional basis functions were developed by Sherwin and Karniadakis through mapping hexahedral bases onto a tetrahedron [50],[25].

Unstructured meshes lack the rotational symmetry therefore basis functions are formed by the application of a warped tensor product. Thus an unstructured expansion is written as:

$$\varphi_{pqr}(\eta_1, \eta_2, \eta_3) = \psi_p^a(\eta_1)\psi_{pq}^b(\eta_2)\psi_{pqr}^c(\eta_3) \qquad (2\text{-}26)$$

where $\psi_p^a(\eta_1), \psi_{pq}^b(\eta_2) and \psi_{pqr}^c(\eta_3)$ are one, two and three dimensional tensors respectively, such that these functions are called orthogonal principal functions which are made of Jacobi polynomials. The orthogonality of the basis functions in the Legendre inner product is assured with these Jacobi polynomials, which can be found through a recursive relation. The characteristic of this basis function is, the lower order expansion set P are subsets of the higher order expansion set $P+1$ which are also called hierarchical modal bases. Another important property of this basis function is an interior/ boundary decomposition. Interior mode is defined only in the interior of an element and is zero on the boundaries while boundary modes have non-zero contributions on the boundaries. Further boundary modes are decomposed into vertex, edge and face modes such that a vertex mode is a linear function defined as being one at its vertex and zero at all the other vertices, an edge mode is defined as functions ranging from quadratic to order P ,which are defined on its edge and are zero on the other edges and vertices, a face mode is defined as a function ranging from quadratic to order $P-1$ which is defined at its face and zero on the other faces, edges and vertices. This decomposition as well as the properties of hierarchical expansions lead to efficient conformity enforcement between elements.

2.5 Elemental Operations

An approximate solution is given by summing the basis functions with their respective coefficients over all elements:

$$u^{\delta} = \sum_{k}^{N^{elem}} \sum_{i}^{N^{\mathrm{mod}\,es}} \hat{u}_i \varphi_i \tag{2-27}$$

To evaluate integrals, method of weighted residuals can be used. Integration can be approximated using Gaussian quadrature on an interval [-1, 1]:

$$\int_{-1}^{1} u(\xi)d\xi = \sum_{i=0}^{Q-1} w_i u(\xi_i) + R(u) \tag{2-28}$$

where ξ_i are the respective quadrature points and w_i are the corresponding weights. Residual term $R(u)$ becomes zero when sufficient numbers of quadrature points are used. By dropping the reference coordinate system altogether in the spectral element method, all of the elemental operations performed purely in the collapsed coordinate system and afterward mapped onto the physical coordinate system. A simple linear element in the physical coordinate system can be mapped from the collapsed coordinate system as:

$$x(\eta_1,\eta_2,\eta_3) = \hat{x}_A\varphi_A + \hat{x}_B\varphi_B + \hat{x}_C\varphi_C + \hat{x}_D\varphi_D \tag{2-29}$$

where x denotes the coordinates of the respective vertices. The integration in the physical coordinate system is given by:

$$\int_{\Omega} u(x,y,z)\partial\Omega = \int_{-1}^{1}\int_{-1}^{1}\int_{-1}^{1} u^{\delta}(\eta_1,\eta_2,\eta_3)\left|\frac{\partial(x,y,z)}{\partial(\eta_1,\eta_2,\eta_3)}\right| d\eta_1 d\eta_2 d\eta_3 \tag{2-30}$$

$$\int_{\Omega} u(x,y,z)\partial\Omega = \sum_{i=0}^{Q_1-1}\sum_{j=0}^{Q_2-1}\sum_{k=0}^{Q_3-1} u^{\delta}(\eta_{1i}^{0,0},\eta_{2j}^{0,0},\eta_{3k}^{0,0}) J_{x\to\eta} w_i^{0,0} w_j^{0,0} w_k^{0,0} \tag{2-31}$$

where Q_1, Q_2, Q_3 are the number of quadrature points required in each collapsed coordinate direction. Furthermore it is seen that the Jacobian between the physical and collapsed coordinate systems and weights are evaluated at the quadrature points. To avoid the singular points, different integration rules are used in different coordinate direction. In the η_1 direction, Gauss-Labatto-Jacobi quadrature rule is used where no constraint exist due to singular points (i.e. vertices A and B). The quadrature points in

this direction are defined by $\eta_{1i}^{0,0}$ and the points are the roots of the Jacobi polynomial. In η_2 and η_3 directions, a Gauss–Radau-Jacobi quadrature rule is used, where a constraint exists at vertices C and D (i.e.: $\eta_2, \eta_3 = 1$) due to singularity. Therefore this rule includes only the end point -1 and does not include the other end point 1 to avoid evaluation at the singular vertices. The quadrature points $\eta_{2j}^{0,0}$ *and* $\eta_{3k}^{0,0}$ are the roots of the respective Jacobi polynomials.

The next main elemental operation is the differentiation. It is needed in the numerical evaluation of the derivatives of the basis functions which are approximated by the collocation differentiation approach applied to the physical space. Approximate solution can be represented by Lagrange polynomials:

$$u^{\delta}(\xi_k) = \sum_{i=0}^{N^{\mathrm{mod}\,es}} \varphi_i(\xi_k)\hat{u}_i = \sum_{j=0}^{N^{quad}} h_j(\xi_k) u^{\delta}(\xi_j) \tag{2-32}$$

where $h_j(\xi_k)$ is the Lagrange polynomial defined at a given quadrature point ξ_j and evaluated at the quadrature point ξ_k and $u^{\delta}(\xi_j)$ is the approximate solution which is pre calculated at the given quadrature point. Differentiation of the approximate solution in the physical space can be represented as:

$$\frac{\partial u^{\delta}(\xi_{pqr})}{\partial \xi_1} = \sum_{i=0}^{Q_1}\sum_{j=0}^{Q_2}\sum_{k=0}^{Q_3} \frac{\partial h_i(\xi_{1p})}{\partial \xi_1} h_j(\xi_{2q}) h_k(\xi_{3r}) u^{\delta}(\xi_{ijk}) \tag{2-33}$$

We can simplify the derivative evaluation by a Lagrange polynomial, which is defined at only one point and zero everywhere else:

$$\frac{\partial u^{\delta}}{\partial \xi_1}(\xi_{1p},\xi_{2q},\xi_{3r}) = \sum_{i=0}^{Q_1} \left.\frac{\partial h_i}{\partial \xi_1}\right|_{\xi_{1p}} u^{\delta}(\xi_{1i},\xi_{2q},\xi_{3r})$$

$$\frac{\partial u^{\delta}}{\partial \xi_2}(\xi_{1p},\xi_{2q},\xi_{3r}) = \sum_{j=0}^{Q_2} \left.\frac{\partial h_j}{\partial \xi_2}\right|_{\xi_{2q}} u^{\delta}(\xi_{1p},\xi_{2j},\xi_{3r}) \qquad (2\text{-}34)$$

$$\frac{\partial u^{\delta}}{\partial \xi_3}(\xi_{1p},\xi_{2q},\xi_{3r}) = \sum_{k=0}^{Q_3} \left.\frac{\partial h_k}{\partial \xi_3}\right|_{\xi_{3r}} u^{\delta}(\xi_{1p},\xi_{2q},\xi_{3k})$$

Quadrature points $(\xi_{1i},\xi_{2j},\xi_{3k})$ are chosen to be the same as those for integration, that is, the Gauss-Labatto-Jacobi distribution for η_1 direction, while in η_2 and η_3 directions, the Gauss-Radau-Jacobi distribution are used. In this approach also, derivatives are not defined at singularities similar to integration.

To reduce the operation count significantly, differentiation is simplified greatly through derivatives in the collapsed coordinate system where the derivatives of the modal basis functions are pre-calculated and then changed through the chain rule to the physical coordinate system such that:

$$\frac{\partial u}{\partial \eta_1}(\eta_{1i},\eta_{2i},\eta_{3i}) = \sum_{pqr}^{M} \hat{u}_{pqr} \frac{\partial \varphi_{pqr}}{\partial \eta_1}(\eta_{1i},\eta_{2i},\eta_{3i})$$

$$\frac{\partial u}{\partial x} = \frac{\partial u}{\partial \eta_1}\frac{\partial \eta_1}{\partial x} + \frac{\partial u}{\partial \eta_2}\frac{\partial \eta_2}{\partial x} + \frac{\partial u}{\partial \eta_3}\frac{\partial \eta_3}{\partial x} \qquad (2\text{-}35)$$

Depending on efficiency, we can choose the method for derivative calculation; i.e., if the solution and its derivatives are needed (such as a convection operator), the collocation method performs this operation more efficiently.

2.6 Elemental Matrices

In order to assemble a system of algebraic equations, we need to construct different elemental matrices.

Mass matrix M is an important operational matrix, which appears in the weak formulation as an inner product of two basis functions:

$$M = \int_{\Omega} \varphi_i \varphi_j \partial\Omega \tag{2-36}$$

Another frequently encountered matrix is the stiffness matrix A which appears in the weak formulation as an inner product of the derivative of basis functions:

$$A = \sum_{n=1}^{3} \int_{\Omega} \frac{\partial \varphi_i}{\partial x_n} \frac{\partial \varphi_j}{\partial x_n} \partial\Omega \tag{2-37}$$

Derivative matrix D_n represents in the weak formulation as an inner product of the trial function with a derivative of the pressure basis functions:

$$D_n = \int_{\Omega} \varphi_i^v \frac{\partial \varphi_j^p}{\partial x_n} \partial\Omega \quad , \; n = 1,2,3 \tag{2-38}$$

Convection operator $C(u)$ appears in the weak formulation as the inner product of the trial function with the velocity field and the derivative of the velocity field:

$$C_\beta(\hat{u}) = \sum_{\alpha=1}^{3} \varphi_i \varphi_j (\hat{u}_\alpha)_j \frac{\partial \varphi_k}{\partial x_\alpha} (\hat{u}_\beta)_k \qquad \beta = 1,2,3 \tag{2-39}$$

This convection operator is discretized by using explicit third order multi-step schemes defined by Cardenas [02] such that:

$$C_\beta(\hat{u}^{n+1}) = \tfrac{8}{3} C_\beta(\hat{u}^n) - \tfrac{7}{3} C_\beta(\hat{u}^{n-1}) + \tfrac{2}{3} C_\beta(\hat{u}^{n-2}) \tag{2-40}$$

where superscripts n represent the time step. In the code, at each time step only the integration of the convection operator is performed on the velocity values from the previous time step, while the two other terms are retrieved from memory.

The rotational matrix R_n is an inner product of rotational term $\nabla \times \nabla \times u$ with the derivative of a pressure basis functions. The resulting three rotational matrices are:

$$R_1 u = \int_\Omega \left[\frac{\partial \varphi}{\partial z} \frac{\partial^2 \varphi}{\partial x \partial z} + \frac{\partial \varphi}{\partial y} \frac{\partial^2 \varphi}{\partial x \partial y} - \frac{\partial \varphi}{\partial x} \left(\frac{\partial^2 \varphi}{\partial y^2} + \frac{\partial^2 \varphi}{\partial z^2} \right) \right] \partial\Omega \cdot u$$

$$R_2 v = \int_\Omega \left[\frac{\partial \varphi}{\partial x} \frac{\partial^2 \varphi}{\partial x \partial y} + \frac{\partial \varphi}{\partial z} \frac{\partial^2 \varphi}{\partial y \partial z} - \frac{\partial \varphi}{\partial y} \left(\frac{\partial^2 \varphi}{\partial x^2} + \frac{\partial^2 \varphi}{\partial z^2} \right) \right] \partial\Omega \cdot v \qquad (2\text{-}41)$$

$$R_3 w = \int_\Omega \left[\frac{\partial \varphi}{\partial x} \frac{\partial^2 \varphi}{\partial x \partial z} + \frac{\partial \varphi}{\partial y} \frac{\partial^2 \varphi}{\partial y \partial z} - \frac{\partial \varphi}{\partial z} \left(\frac{\partial^2 \varphi}{\partial x^2} + \frac{\partial^2 \varphi}{\partial y^2} \right) \right] \partial\Omega \cdot w$$

where the first derivative $\frac{\partial \varphi}{\partial x_i}$ is evaluated by employing the derivative of the basis functions and the second derivative $\frac{\partial^2 \varphi}{\partial x_i \partial x_j}$ is obtained by employing collocation differentiation and the derivatives of the basis functions.

Once all of these matrices and operators are built, the resulting equations are given by:

$$\left[\frac{A}{\mathrm{Re}} + \frac{3M}{2\Delta t} \right] \underline{\hat{u}}^{n+1} = f^{n+1} - D\left(2p^n - p^{n-1}\right) - C\left(\hat{u}^n, \hat{u}^{n-1}, \hat{u}^{n-2}\right) - \frac{M}{\Delta t}\left(2\hat{u}^n - \tfrac{1}{2}\hat{u}^{n-1}\right) \qquad (2\text{-}42)$$

$$Ap^{n+1} = \tilde{f}^{n+1} - \tilde{C}(\hat{u}_i^n, \hat{u}_i^{n-1}, \hat{u}_i^{n-2}) - \tfrac{1}{\mathrm{Re}}\left[R_i \hat{u}_i^{n+1}\right] \qquad (2\text{-}43)$$

where trial functions of $\tilde{f}$ and $\tilde{C}$ are pressure derivative basis functions in equation (2-43). Then equation (2-42) is solved to obtain the vector of velocity coefficients and the equation (2-43) is solved to obtain the pressure coefficients at each time step.

2.7 Transformation

In the modal basis functions, coefficients of the basis functions do not represent the physical nodal point value, thus transformations between the coefficient and physical spaces are introduced. They are backward transformation which means mapping the modal basis functions onto the physical space and forward transformation where conversely mapping a physical space onto the modal space.

The backward transformation represents the physical approximate solution by the summation of all modal basis functions with their respective coefficients. This is given by:

$$u^{\delta}(\eta_1,\eta_2,\eta_3) = \sum_{i=1}^{N^{dof}} \hat{u}_i \varphi_i(\eta_1,\eta_2,\eta_3) \tag{2-44}$$

where $\hat{u}$ is the vector of coefficients and φ_i are the basis functions evaluated at specified points. While we evaluate approximate solution at discrete or nodal points in the physical space, the number of discrete points should be less than or equal to the number of modes. As long as the coefficient space solution is known, physical space solution can be found in the post processing functions by considering the number of nodes is equal to the number of modes.

More over the forward transformation projects the physical values onto the coefficient space. These coefficients can be represented by the following equation:

$$\sum_{pqr} \left(\varphi_{ijk}, \varphi_{pqr}\right) \hat{u}_{pqr} = \left(\varphi_{ijk}, f\right) \tag{2-45}$$

where f is the physical space representation of a function evaluated at the quadratic points. The above coefficients of the modes $\hat{u}$ can be calculated via the inversion of the

mass matrix onto the inner product of the forcing function f with the basis functions. This forward transformation will be used in the subsection of Dirichlet boundary condition.

2.8 Global Assembly

Global assembly is a mapping from local domain to the global domain to form global continuous expansion bases. The boundary/interior decomposition of basis functions ensure that only the boundary modes are defined at the elemental boundary, while the interior basis functions are zero at the boundaries. The global-local mapping needs only to be performed at the boundaries as only those modes share a neighbor. Interior modes are automatically global modes as they do not have any boundary interaction. The decomposition of the domain through the mesh ensures that global data is spread between the neighboring elements. Local and global degrees of freedom are denoted by the vectors $\hat{u}^e$ and $\hat{u}_g$ respectively. A mapping vector map_i^k is formed to return the global degree of freedom for a mode number i and an element number k. The numbering of the global degrees of freedom is arranged such that vertex modes are labeled first, followed by edges, faces and interior modes.

A scatter operation is defined as the mapping from global modes to the local modes:

$$u_i^k = \hat{u}_g\left[map_i^k\right] \tag{2-46}$$

An opposite operation called the global assembly is defined to be the mapping from the local modes to the global modes becomes:

$$\hat{u}_g\left[map_i^k\right] = \sum_k^{N^{elem}} \sum_i^{N^{modes}} \hat{u}_i^k \tag{2-47}$$

2.9 Continuity enforcement

When assembling local modes to form continuous global expansion functions, continuity should be enforced due to the lack of rotational symmetry of the bases in the second order partial differential equations. To enforce continuity, two constraints need to be satisfied: the general orientation of the local coordinate system has to align and the directions of the coordinate systems have to match. In an element, the vertices A, B, C and D are defined at the collapsed coordinates $(-1,-1,-1), (1,-1,-1), (-1,1,-1)$ and $(-1,-1,1)$ respectively. This procedure first starts with the orientation constraint which is satisfied through local renumbering operation on vertex modes. Assign the lowest global number in an element to vertex D and then the second lowest global number to vertex C. Thus both the η_2 *and* η_3 directions are matched but leave the orientation of the η_1 coordinate system (edge AB) as a final degree of freedom. Thus the orientation of this collapsed coordinate system can be flipped by reversing the global numbering of the vertices A and B. It means that while edges are checked for continuity with their neighbors, vertices A and B numbering is flipped if non-matching coordinates are found. Altogether this implementation enforces the continuity as a pre-processing step and does not require any modifications to the global assembly operation through assigning the above local coordinate systems correctly.

2.10 Compressed Row Storage

The sparseness is important to the choice of solution algorithm and the storage requirement of each matrix. The sparseness of a matrix is increasing with the expansion order increase. Storing the full matrices and performing operations on these full matrices are computationally expensive therefore all the matrices used in this code are stored by compressed row storage. This method keeps only the non zero entries of a matrix and uses three vectors; V, C and R. Vector V stores the non-zero matrix values as doubles, vector C stores the corresponding column position of the non-zero matrix value as integers, finally vector R stores the ranges of indices of the V vector indicating values in a given row as integers. The following algorithm is used to calculate matrix-vector product efficiently.

for $i = 1 : n$

for $j = R[i] : R[i+1] - 1$

$a[i] = V[j] \times b[C[j]]$

The above algorithm performs operations only on non-zero values compared to the original matrix which uses all values of the matrix.

2.11 Schur Complement Method

Equations (2-42) and (2-43) are modified to the following form:

$$\overline{H}\hat{u} = \overline{f} \tag{2-48}$$

$$\overline{A}\hat{p} = \overline{g} \tag{2-49}$$

where $\overline{f} = \left[f^{n+1} - D(2p^n - p^{n-1}) - C(\hat{u}^n, \hat{u}^{n-1}, \hat{u}^{n-2}) - \frac{M}{\Delta t}\left(2\hat{u}^n - \frac{1}{2}\hat{u}^{n-1}\right)\right]$,

$\overline{g} = \left[\tilde{f}^{n+1} - \tilde{C}(\hat{u}_i^n, \hat{u}_i^{n-1}, \hat{u}_i^{n-2}) - \frac{1}{\mathrm{Re}}\left[R_i \hat{u}_i^{n+1}\right]\right]$ and $\overline{H} = \left(\frac{A}{\mathrm{Re}} + \frac{3M}{2\Delta t}\right)$. Here $\overline{H}$ and $\overline{A}$ are Helmholtz and Stiffness matrices respectively. In the velocity and pressure field calculations, we need to take the inverses of Helmholz and Stiffness matrices. This operation is done by using Schur complement method where interior solutions can be decoupled from the boundary solutions naturally. In Schur complement method, a matrix can be represented as:

$$\overline{H} = \begin{bmatrix} H_b & H_c \\ H_c^T & H_i \end{bmatrix} \tag{2-50}$$

where H_b, H_c, H_i are boundary-boundary, boundary-interior, interior-interior interaction matrices respectively. Therefore equation (2-48) can be written as:

$$\begin{bmatrix} H_b & H_c \\ H_c^T & H_i \end{bmatrix}\begin{bmatrix} \hat{u}_b \\ \hat{u}_i \end{bmatrix} = \begin{bmatrix} f_b \\ f_i \end{bmatrix} \tag{2-51}$$

where the subscripts b, i denote boundary and interior modes respectively. By performing a Guass elimination step, the above system can be solved in three steps:

$$\tilde{u}_i = H_i^{-1} f_i \tag{2-52}$$

$$\left(H_b - H_c H_i^{-1} H_c^T\right)\hat{u}_b = f_b - H_c \tilde{u}_i \tag{2-53}$$

$$\hat{u}_i = \tilde{u}_i - H_i^{-1} H_c^T u_b \tag{2-54}$$

In the first step a local interior solution is obtained by the local elemental inverse of interior matrix through Cholesky decomposition. In the second step, global Schur matrix

$\left(H_b - H_c H_i^{-1} H_c^T\right)$ is inverted to obtain the boundary solution. Finally, the previous local interior solution is corrected to obtain interior solution.

Numerical solution of Navier-Stokes equations is computationally expensive. This is overcome by parallelization of the code by separating the problem into smaller portions. This means all the processors need to communicate with the sub-solution to obtain a global solution. This is done by domain decomposition METIS library developed by G.Karypis [24] which breaks up a computational domain into non-overlapping sub-domains by assigning specific elements to a given processor. This domain decomposition algorithm is demonstrated on two processors to solve equation (2-53):

$$[S]\tilde{u} = \tilde{f} \tag{2-55}$$

where S and $\tilde{f}$ are global Schur matrix and modified forcing vector respectively.

Global Schur system in two processors is:

$$\begin{bmatrix} S_{ss} & S_{1s} & S_{2s} \\ S_{1s}^T & S_{11} & 0 \\ S_{2s}^T & 0 & S_{22} \end{bmatrix} \begin{bmatrix} \tilde{u}_s \\ \tilde{u}_1 \\ \tilde{u}_2 \end{bmatrix} = \begin{bmatrix} \tilde{f}_s \\ \tilde{f}_1 \\ \tilde{f}_2 \end{bmatrix} \tag{2-56}$$

where S_{11}, S_{22} are local components and S_{1s}, S_{2s} are shared components of the global Schur matrix. Similarly forcing and solution vectors also have local and shared contribution. By performing two Gauss elimination steps, the above system can be solved in three steps:

$$\tilde{u}_1 = S_{11}^{-1}\tilde{f}_1 \text{ and } \tilde{u}_2 = S_{22}^{-1}\tilde{f}_2 \tag{2-57}$$

$$\left[S_{ss} - S_{1s}S_{11}^{-1}S_{1s}^T - S_{2s}S_{22}^{-1}S_{2s}^T\right]\tilde{u}_s = \tilde{f}_s - S_{1s}\tilde{u}_1 - S_{2s}\tilde{u}_2 \tag{2-58}$$

$$\tilde{u}_1 = \tilde{u}_1 - S_{11}^{-1} S_{1s}^T \tilde{u}_s \quad \text{and} \quad \tilde{u}_2 = \tilde{u}_2 - S_{22}^{-1} S_{2s}^T \tilde{u}_s \tag{2-59}$$

The first step solves for all intermediate local solutions, performed locally on each processor. Then the second step is solved through a global conjugate gradient method to obtain shared solution. The final step updates the local solution based on the shared solution.

Schur complement method is again used to equation (2-57) to find local inverse, which is composed of vertex, edge and face contributions such that:

$$\begin{bmatrix} L_{vv} & L_{ve} & L_{vf} \\ L_{ve}^T & L_{ee} & L_{ef} \\ L_{vf}^T & L_{ef}^T & L_{ff} \end{bmatrix} \begin{bmatrix} \tilde{u}_{1v} \\ \tilde{u}_{1e} \\ \tilde{u}_{1f} \end{bmatrix} = \begin{bmatrix} \tilde{f}_{1v} \\ \tilde{f}_{1e} \\ \tilde{f}_{1f} \end{bmatrix} \tag{2-60}$$

This local system is solved to obtain vertex, edge and face solution by Gauss elimination steps and Cholesky decomposition. The required computational resources are optimized by employing Schur complement method at the pre-processing step and storing sparse matrices by compressed row storage method.

2.12 Preconditioning

In order to achieve higher computational efficiency, a study was done to determine which calculation consumes the most computational time. It showed that velocity as well as pressure solve steps require the largest proportion of time in each time step calculation. The shared global conjugate gradient solves, requires most time and thus requires most iteration count. The significant factor to determine the number of required iterations to solve a system is called the condition number:

$$N_{iteraton} \propto [\text{condition number}]^{1/2} \tag{2-61}$$

Therefore a preconditioning is performed to the given system to reduce the condition number. This is achieved by multiplying the matrix system $\overline{H}\hat{u} = \overline{f}$ with a preconditioning matrix K^{-1} which is the inverse of the diagonal component of the original matrix, such that the new system becomes:

$$K^{-1}\overline{H}\hat{u} = K^{-1}\overline{f} \tag{2-62}$$

This method is called Jacobi preconditioning and scales the original matrix by this preconditioning matrix to reduce the condition number. This method improved the efficiency of the code by reducing the solve time for velocity and pressure steps remarkably.

2.13 Equal ordered P/P formulation

Navier-Stokes equation is solved by an equal order P/P formulation for velocity and pressure which shows higher accuracy in both solutions because this method do not exhibit spurious pressure modes in the rotational formulation. If we use the lesser order for the pressure than the velocity, convergence rate will be lower for the pressure than the velocity. Through this method instability of Reynolds number is reduced. This means allows for solving high Reynolds number flows on a given mesh. However, in this thesis we used this formulation only for some validation procedures.

2.14 Time-step size for temporal discretization

Temporal discretization of explicit scheme of the convection operator is stable, if the following condition is satisfied such that:

$$\Delta t \le \Delta t_{cri} = \min\left(\frac{h'}{u'}\right) * 0.723 \tag{2-63}$$

where $h' = |x_b - x_a|$ and $u' = \frac{|u.(x_b - x_a)|}{|x_b - x_a|}$. Here a *and* b are minimum over all modes and minimum over neighbor modes respectively. To determine the adequate time-step size Δt, the ratio $\left(h'/u'\right)$ should be a minimum value. Therefore we need to find the minimum length h' and the maximum velocity u' in the entire computational domain. Thus, the minimum length is approximately given by:

$$h'_{\min} \approx \frac{1}{P}\left(\frac{|(\underline{a}-\underline{d})\cdot(\underline{b}-\underline{d})\times(\underline{c}-\underline{d})|}{6}\right)^{1/3} \tag{2-64}$$

where $\underline{a},\underline{b},\underline{c}$ *and* $\underline{d}$ are coordinates represented as vectors at the vertices of the smallest tetrahedron in the geometry of interest and P is the order of the Jacobi polynomials. To allow for numerical errors, evaluated time step could be multiplied with a safety factor. Euler backward implicit scheme is used to discretize the unsteady term in the Navier-Stokes equation which is unconditionally stable therefore Δt is set only by convection operator.

2.15 Post-processing

In order to post process the high order spectral element data, available lower order visualization software packages are used such as Tecplot and Opendx. To capture the higher accuracy of the elements, a method is developed which fills the higher order element with linear elements. For example, expansions order P=3 have 20 modes which are distributed at equal distances in the tetrahedron. These modal points are linked to form 26 tetrahedrons. Although the above mentioned procedure allows for visualizations,

further post processing subroutines are needed to capture the high accuracy data. These operations usually require respective collapsed coordinates from a given physical point distribution. To find this corresponding collapsed coordinates, a non-linear Newton method is employed. Then the obtained collapsed coordinates can be used in the backward transformation to determine the physical solution at the given point. Further complexities arise in the derivative calculations where singularities exist at the vertices C and D and the edge CD. In this case, the non linear Newton method cannot be used, and these vertices C and D are checked separately to avoid this problem. At the same time on the edge CD, a one dimensional root finding algorithm is used in the η_3 direction.

Chapter 3

Boundary and Initial Conditions for Validation of the Code

3.1 Boundary Conditions

The boundary condition issue for the Navier-Stokes equation is quite delicate and can significantly affect the solution. The simplest and most common boundary condition is 'no penetration and no-slip' at a solid wall (or an object). Here the normal and tangential velocity components must agree with those at the wall (or object). Another important boundary condition is arbitrary slip which does not permit penetration. Due to the incompressibility constraint, flow must be parallel to the boundary for the slip condition.

For numerical implementation, Dirichlet boundary conditions which fit known values of the flow components are used to specify velocities such as no-slip at the wall or inlet profiles (i.e. parabolic profile for the channel flows, Blasius profile for the boundary layer flows). Concerning the outflow and far-field boundary, many different approaches exist. The implementation of these boundary conditions in spectral element method is an important operation which will be described in the following sub sections.

3.1.1 Dirichlet Boundary Condition

This boundary condition (g_D) is imposed on a partial differential equation which specifies the values a solution needs to take at the boundary of the domain. This is implemented in the spectral element method by decomposing the domain into a homogenous part (u^H) where the solution has to be found and a non-homogenous part

(u^D) where the known values have to be enforced. Hence, known values (u^D) are condensed out from the left hand side of the system and subtracted from the right hand side to solve for u^H. A consistent local method is used to project a Dirichlet boundary condition on the coefficient space by ensuring continuity. As we know, boundary is decomposed into vertex, edge and face modes which are projected locally in every element to get the required contributions of g_D in three steps. Firstly, the coefficient of the vertex mode is set by the given physical value boundary condition because a vertex is unity at its respective vertex and zero at all the other vertices. This is called vertex projection. Secondly, only edge contributions are projected onto edge modes locally. As we stated earlier, edge modes have a value at its own edge and are zero on all the other edges and vertices. However, to ensure only edge contributions are projected, the vertices which are on the end points of the edge are subtracted from the projected boundary condition g_D to ensure continuity. It is shown below for an edge AB:

$$u^{\delta} = \sum_{(pqr)AB} \hat{u}^e_{AB} \varphi_{AB} = g_D - \hat{u}^e_A \varphi_A - \hat{u}^e_B \varphi_B \tag{3-1}$$

A weak formulation is formed to solve the edge modes at the coefficient space:

$$\left(\varphi_{i00}, \sum_{i=1}^{P-1} \hat{u}^e_{i00} \varphi_{i00} \right) = \left(\varphi_i, g_D - \hat{u}^e_{000} \varphi_{000} - \hat{u}^e_{P00} \varphi_{P00} \right) \tag{3-2}$$

Inversion of a local one dimensional mass matrix is constructed to solve for edge mode coefficients. Here in order to do integration, the Gauss-Jacobi quadrature rule is used only at edge modes.

Finally, only face contributions are projected locally onto face modes where vertex and edge modes are condensed out, i.e. subtracted from the g_D boundary condition to ensure continuity. This is shown below for a face ABC:

$$u^{\delta} = \sum_{(pqr)ABC} \hat{u}^{e}_{ABC}\varphi_{ABC} = \begin{pmatrix} g_D - \hat{u}^{e}_{A}\varphi_{A} - \hat{u}^{e}_{B}\varphi_{B} - \hat{u}^{e}_{C}\varphi_{C} - \sum_{(pqr)AB} \hat{u}^{e}_{AB}\varphi_{AB} - \sum_{(pqr)BC} \hat{u}^{e}_{BC}\varphi_{BC} \\ - \sum_{(pqr)AC} \hat{u}^{e}_{AC}\varphi_{AC} \end{pmatrix} \quad (3\text{-}3)$$

Again, a weak formulation is found to solve for face modes at the coefficient space:

$$\left(\varphi_{ij0}, \sum_{p=1}^{P-1}\sum_{q=1}^{Q-1} \hat{u}^{e}_{pq0}\varphi_{pq0}\right) = \begin{pmatrix} \varphi_{ij0}, g_D - \hat{u}^{e}_{000}\varphi_{000} - \hat{u}^{e}_{P00}\varphi_{P00} - \hat{u}^{e}_{0P0}\varphi_{0P0} \\ -\sum_{p=1}^{P-1} \hat{u}^{e}_{p00}\varphi_{p00} - \sum_{q=1}^{Q-1} \hat{u}^{e}_{Pq0}\varphi_{Pq0} - \sum_{q=1}^{Q-1} \hat{u}^{e}_{0q0}\varphi_{0q0} \end{pmatrix} \quad (3\text{-}4)$$

Another inversion of local two dimensional mass matrix is formed to solve for face modes. Gauss-Jacobi quadrature rule is again used to perform integration locally just on the face modes.

3.1.2 Outflow Boundary Condition

Concerning the outflow boundary, many conditions can be applied such as linearized convective equation or Navier-Stokes equation without pressure gradient term [09] or open boundary condition [12] or stream-wise periodicity [52] or buffer-domain technique[22],[31] etc. However, in this numerical study, we use an open boundary condition which can be written as a passive open boundary condition. This approach works better than any other alternative form demonstrated by Gresho [12]. This is given by:

$$\frac{\partial(\cdot)}{\partial n} = 0 \tag{3-5}$$

Thus, we could use both $\frac{\partial u_n}{\partial n} = 0$ and $\frac{\partial u_\tau}{\partial n} = 0$ as boundary conditions at the outlet.

3.1.3 Free surface Boundary Condition

An interface between two fluids (e.g., gas and liquid) is often referred to as a free surface. The reason for the "free" designation arises from the large difference in the densities of both fluids. Generally the inertia of the lower density fluid can be ignored compared to the larger density fluid. In this sense the higher density fluid moves independently or freely with respect to the lower density fluid. This boundary surface is not constrained, in other words, the flow at this boundary is not adversely affected by environment thus the flow passes through this boundary without any refraction.

Flows typically dealing with these free surfaces, force (per unit area) balance boundary condition is used, also referred as specified traction on or at the boundary. This is obtained from the true momentum balance equation (2-3) in the stress-divergence form. This stress divergence term leads to a natural boundary condition which represents true physical force, and they are on the planar boundaries stated as:

$$\begin{aligned} F &= -n.\pi = -\pi.n = \mu\left[\nabla u + (\nabla u)^T\right].n - Pn \\ F &= \mu\left(\frac{\partial u}{\partial n} + \nabla u_n\right) - Pn \end{aligned} \tag{3-6}$$

where $u_n \equiv n.u$ is the normal velocity.

For simplicity this boundary condition is expressed in two dimensional forms at a planar boundary as:

$$F_n = n.F = 2\mu \frac{\partial u_n}{\partial n} - P \tag{3-7}$$

$$F_\tau = \tau.F = \mu\left(\frac{\partial u_\tau}{\partial n} + \frac{\partial u_n}{\partial \tau}\right) \tag{3-8}$$

where equations (3-7) and (3-8) are written in the normal and tangential directions respectively.

The above boundary condition causes problems because the proper values are usually not known for F_n and F_τ, the pressure appears in the normal direction and a term $\frac{\partial u_n}{\partial \tau}$ appears in the tangential direction. This term $\frac{\partial u_n}{\partial \tau}$ can be removed by omitting the term $(\nabla u)^T$ by considering the simpler momentum balance equation (2-9) where we deal with the incompressible flows. Therefore, a natural boundary condition associated with the simpler Navier-Stokes equation becomes:

$$f_n = \mu \frac{\partial u_n}{\partial n} - P \tag{3-9}$$

$$f_\tau = \mu \frac{\partial u_\tau}{\partial n} \tag{3-10}$$

where f_n and f_τ are new traction force components. From the recent mathematical analysis, these boundary conditions are useful from a point of view of stability [35], [14]. The above stated boundary conditions are not completely natural in our discretized weak formulation of the Navier-Stokes equation (2-18). Further strengthening this argument that the pressure gradient should be integrated by parts but the present work considered weak form of pressure gradient without integrating by parts. Therefore according to our weak formulation (2-18), pressure term in the normal direction is excluded in equation

(3-9) such that the latest traction force components can be written in the non-dimensionalized form as:

$$\tilde{f}_n = 1/\mathrm{Re}\,\frac{\partial u_n}{\partial n} \tag{3-11}$$

$$\tilde{f}_\tau = 1/\mathrm{Re}\,\frac{\partial u_\tau}{\partial n} \tag{3-12}$$

The above latest traction force components are used in a situation where free surfaces are encountered in the problems of interest.

3.1.4 Methodology to construct Surface Matrices in the SEM

Implementing the above cited boundary conditions in sections 3.1.2 and 3.1.3 and non-Dirichlet boundary conditions in spectral element method is a trivial operation because boundaries in three dimensions are represented on the faces of the tetrahedron. Therefore we have to construct surface matrices at these boundaries

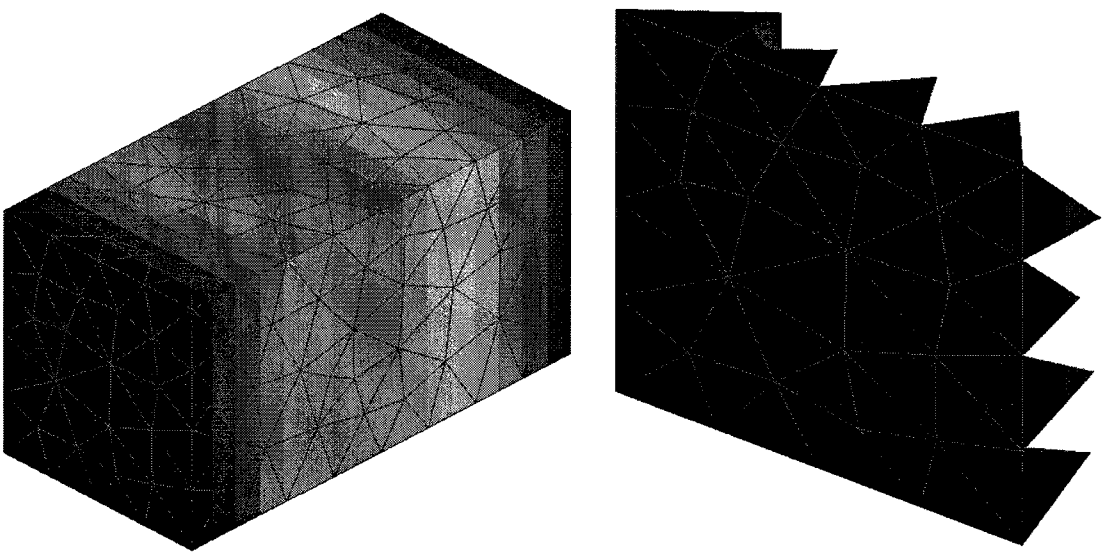

Figure 3-1. Elements are chosen in the domain where only one face of the tetrahedron lies on the outlet boundary

Note that our geometry of interest consist of planar (straight) surfaces at each boundary where one face of a tetrahedron lies on this planar surface and the balance resides inside the computational domain as shown in Figure 3-1. Finding these faces and constructing two dimensional expansion bases at these faces are nevertheless challenging operations. These two dimensional bases are found at the quadrature points on the face of the tetrahedron to perform integration. As we stated in the previous chapter, in a tetrahedron, quadrature point distribution was given by $(\eta_{1i}, \eta_{2j}, \eta_{3k})$ and different quadrature rules are used in the different collapsed coordinate direction. But a face is represented only by two collapsed coordinate directions where third coordinate direction is parameterized at the face as:

$$\begin{aligned} face\ ABC &\equiv (\eta_{1i}, \eta_{2j}, -1) \\ face\ ABD &\equiv (\eta_{1i}, -1, \eta_{3j}) \\ face\ BCD &\equiv (1, \eta_{2i}, \eta_{3j}) \\ face\ ACD &\equiv (-1, \eta_{2i}, \eta_{3j}) \end{aligned} \tag{3-13}$$

In order to perform integration on a face, Gauss-Labatto-Jacobi quadrature rule is used in the η_1 direction and Gauss-Radau-Jacobi quadrature rule is used in the η_2 *and* η_3 directions. This means that both GLJ and GRJ quadrature rules are needed to perform integration on faces ABC and ABD but only GRJ rule is enough to perform integration at faces BCD and ACD.

The created face matrix values are stored in the corresponding locations on the elemental matrices, which correspond to the boundary. These elemental matrices are used to enforce boundary conditions such as outflow and free surfaces.

The Greens theorem is used to validate the constructed face matrices. By performing integration by parts on the weak pressure derivative term $-(v,\nabla p)$ in the weak form of the Navier-Stokes equation (2-18), we obtain a term $-[vpn]_{\partial\Omega}$ at the boundaries. As we mentioned in Chapter 2, space of trial function v is zero at the Dirichlet boundaries where the term $-[vpn]_{\partial\Omega}$ reduces to zero at these boundaries. However, this term $-[vpn]_{\partial\Omega}$ is not zero at outflow or free surfaces or other boundaries.

$$\begin{aligned} -(v,\nabla p) &= -[vpn]_{\partial\Omega} + (p,\nabla v) \\ -(\varphi^{v}_{3D},\varphi'^{p}_{3D})\hat{p} &= -(\varphi^{v}_{2D},\varphi^{p}_{2D})\hat{p} + (\varphi^{p}_{3D},\varphi'^{v}_{3D})\hat{p} \\ \underbrace{-D_{3D}\hat{p}}_{Case\,I} &= \underbrace{-M_{2D}\hat{p} + D_{3D}\hat{p}}_{Case\,II} \end{aligned} \tag{3-14}$$

The flow through a simple channel is chosen to carryout the validation. At the inlet, parabolic profile is applied in the stream-wise direction and other velocity components are set to zero. 'no-slip and no-penetration' conditions are used in the upper and lower walls. Both side walls in the span-wise direction are set to 'slip and no-penetration' condition. At the downstream boundary, passive open boundary condition (3-5) is applied. Zero initial condition is assumed throughout the flow domain.

In the first case, governing equations (2-42 and 2-43) are solved to simulate the parabolic flow through the channel without any changes in the weak pressure derivative term as shown in the left hand side of the equation (3-14). Velocity profiles at the down stream locations and the time (or total number of iterations) needed to reach the steady state solution are reported. These results will be utilized to validate the subsequent case.

In the second case, same governing equations (2-42 and 2-43) are solved but the weak pressure derivative term is replaced with $(p,\nabla v)$ and $-[vpn]_{\partial\Omega}$ as shown in the right hand

side of the equation (3-14) to carryout the validation on the constructed surface matrix. As we stated earlier, the term $-[vpn]_{\partial\Omega}$ reduces to zero only at the Dirichlet boundaries. Therefore, we enforced this condition at the side walls and outlet. This is implemented by constructing two dimensional surface mass matrices at these boundaries. Then the forcing term is formed via multiplying the two dimensional surface mass matrix with the corresponding previous time step pressure solutions. At last the forcing term is subtracted from the right hand side of the Navier-Stokes equation (2-42). Again the velocity profiles and the time required to reach the steady state solution are reported. Continuity and the time required to attain the steady state are same for both cases. Simulation results for both cases justified that the methodology used herein to construct the surface mass matrix can be used to create other types of surface matrices such as derivative and stiffness matrices. These matrices will be needed to implement free surface and outflow boundary conditions in the succeeding sections.

3.2 Initial condition

At $t = 0$, a known flow field is assumed throughout the computational domain. In the spectral element method physical values are projected onto the coefficient space to implement this initial condition.

The residual error can be written as the difference between approximate and exact solution such that:

$$u^{\delta} - u = R(u) \tag{3-15}$$

Then the weak formulation is formed as the inner product such that:

$$\left(v, u^{\delta} - u\right) = \left(v, R(u)\right) = 0 \tag{3-16}$$

The above weak formulation can be solved through the method of weighted residuals. Thus, the problem reduces to the minimization of the inner product of the residual such that it becomes zero. The coefficient space values are solved from the following equation:

$$\left(\varphi_i, \varphi_j\right)\hat{u}_j = \left(\varphi_i, u\right) \tag{3-17}$$

Above system of equation (3-17) is represented in the matrix form as:

$$M\hat{u} = f \tag{3-18}$$

Before inverting the mass matrix, Dirichlet portion of the boundary condition need to be incorporated in the equation (3-18). This means that the Dirichlet boundary values are condensed out from the above system. Thereafter, the coefficients can be found through inverting the mass matrix via multilevel Schur complement method as described in the previous chapter:

$$\hat{u} = M^{-1}\tilde{f} \tag{3-19}$$

3.3 Validation

The computer program use here-in was developed by Niewiadomski to simulate the three dimensional flows with tetrahedral elements [36]. Our primary objective is to verify that the program function properly for our problem of interest. First the boundary conditions of our problem of interest were implemented. Secondly, flow developing along a flat plate is considered for validation. Comparison is carried out with the Blasius solution by applying appropriate boundary and initial conditions in the modal spectral element method.

At the inlet, a small distance away from the leading edge, Blasius profiles are assumed in both the stream wise and wall normal directions rather than considering free stream velocity which creates singularity at the zero incidence of the plate.

$$\begin{aligned} u(0,y,z,t) &= u_B(x_o,y) \\ v(0,y,z,t) &= v_B(x_o,y) \\ w(0,y,z,t) &= 0 \end{aligned} \tag{3-20}$$

At the flat plate, the velocity components are zero. Therefore 'no-slip and no-penetration' condition is employed.

$$\begin{aligned} u(x,0,z,t) &= 0 \\ v(x,0,z,t) &= 0 \\ w(x,0,z,t) &= 0 \end{aligned} \tag{3-21}$$

Both side walls in the span-wise directions, 'arbitrary slip and no-penetration' boundary conditions are applied where span-wise velocity component is specified at the boundary through Dirichlet condition.

$$\begin{aligned} w(x,y,0,t) &= 0 \\ w(x,y,Z,t) &= 0 \end{aligned} \tag{3-22}$$

At the outlet, passive open boundary condition is employed which is naturally included in the weak formulation (2-18).

$$\begin{aligned} \frac{\partial u_n}{\partial n} &= 0 \\ \frac{\partial u_\tau}{\partial n} &= 0 \end{aligned} \tag{3-23}$$

In the Navier-Stokes weak formulation (2-16), Laplacian term could be replaced with $[v, \nabla u.n]_{\partial\Omega}$ and $(\nabla v, \nabla u)$ by integrating by parts. In addition, recall that the space of trial functions v in the Galerkin expansion is zero on the Dirichlet boundary. Therefore at the

Dirichlet boundary, weak Laplacian term $\nu\nabla^2 u$ only reduces to $(\nabla v, \nabla u)$. In our problem of interest, the term $[v, \nabla u.n]_{\partial\Omega}$ is not zero at the outlet. As we explained in the previous section, passive open boundary condition (3-5) is chosen at the outlet boundary where the outflow is considered as never ending one. It means that the boundary term $[v, \nabla u.n]_{\partial\Omega}$ vanishes at the outlet.

At the upper boundary, specified traction force components are applied which is incorporated naturally in the Navier-Stokes equation.

$$\begin{aligned} \tilde{f}_n &= 1/\mathrm{Re}\,\frac{\partial u_n}{\partial n} \\ \tilde{f}_\tau &= 1/\mathrm{Re}\,\frac{\partial u_\tau}{\partial n} \end{aligned} \tag{3-24}$$

This becomes in the weak formulation as:

$$f = 1/\mathrm{Re}\,\nu\frac{\partial \underline{u}}{\partial n} \tag{3-25}$$

The above equation (3-25) is represented in the matrix form as:

$$f = 1/\mathrm{Re}\,D_{2D}\hat{\underline{u}} \tag{3-26}$$

where D_{2D} is a two dimensional derivative matrix. This matrix is constructed at the upper boundary analogous to the two dimensional mass matrix in the previous section to enforce the specified traction boundary condition. This means that the traction force (3-26) is added in the right hand side of the Navier-Stokes equation (2-42) at the upper surface of the domain.

Finally, *initial conditions* are applied at $t = 0$ where Blasius solution at the inlet is assumed in the entire flow field.

$$u(x,y,z,0) = u_B(x_0,y)$$
$$v(x,y,z,0) = v_B(x_0,y) \qquad (3\text{-}27)$$
$$w(x,y,z,0) = 0$$

In the case of a flat plate viscous boundary layer flow, a pressure gradient does not exist in the flow direction [32]. Also no externally applied pressure gradient is specified, so $\frac{\partial p}{\partial x} = 0$ but apparently for a flat plate boundary layer $\frac{\partial p}{\partial y} = 0$. Therefore in our numerical simulation, we dropped the pressure gradient term altogether.

The validation cases ran with the chosen parameters listed in Table 3-1. This procedure is carried out with the following residual stopping criteria.

$$Error = \left| \int_{\Omega} \left(\underline{u}^{n} - \underline{u}^{n-1} \right)^2 \partial\Omega \right| \leq 2 \times 10^{-13} \qquad (3\text{-}28)$$

where superscripts $^{n,\ n-1}$ represent the current and previous time steps respectively.

Case	I	II
Re^*	500	550
P (polynomial order)	3	3
Δx	0.250	0.1000
Δy	0.423	0.2589
Δz	0.250	0.1000
Δt	0.010	0.0010
No. of time steps to reach stopping criteria	2149	15783

Table 3-1.Validation cases parameters

The numerical simulation for the flow developing along a flat plate based on the free stream velocity U_∞ and the inlet displacement boundary layer thickness δ_0^* is compared with the Blasius known solutions for case-I and case-II in the Figure 3-2 through Figure 3-5. Three dimensional computational domain is used to simulate the boundary layer

flow therefore mid plane in the span-wise direction is chosen to carryout the comparison where the span-wise slip wall boundary effects are minimum. Following the comparison, maximum differences between the spectral element results and Blasius solutions at each down stream locations are tabulated in Table 3-2 and Table 3-3 at both side slip walls and the mid plane for both velocity components.

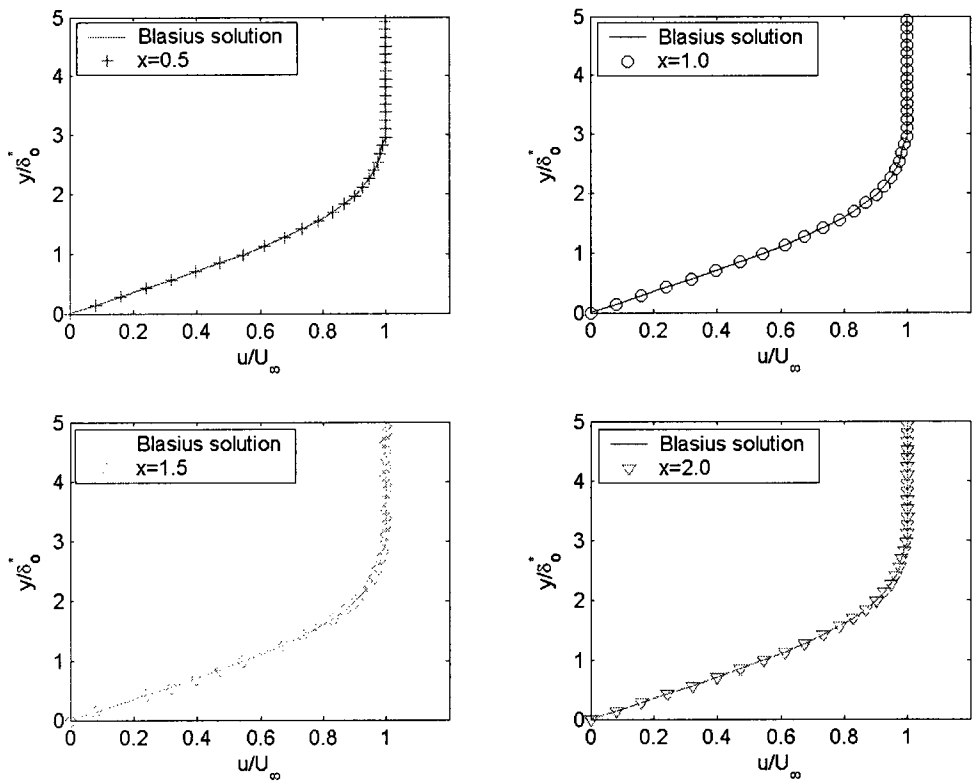

Figure 3-2 Similarity profiles of the stream-wise velocity component at the downstream locations for case-I

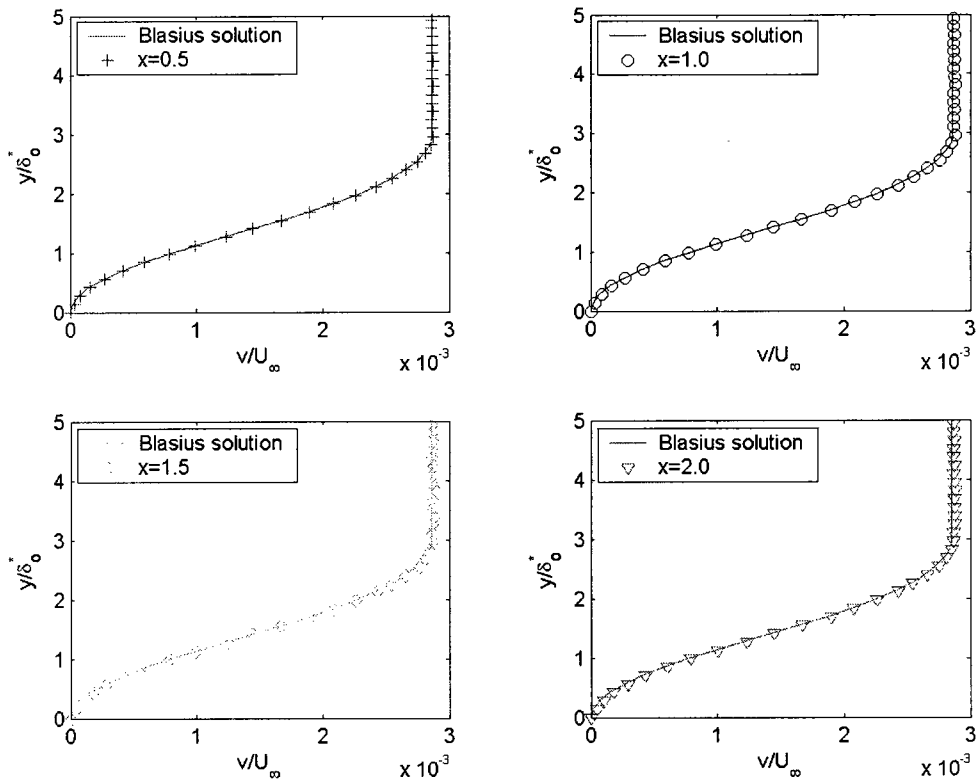

Figure 3-3 Similarity profiles of the wall-normal velocity component at downstream locations for case - I

Location	Velocity components (Maximum error)					
	Slip wall 1 (Z=0)		Mid plane (Z=0.5)		Slip wall 2 (Z=1)	
	u	v	u	v	u	v
0.5	0.001326	0.000014	0.001151	0.000020	0.001251	0.000014
1.0	0.002390	0.000023	0.001802	0.000027	0.002025	0.000021
1.5	0.003516	0.000033	0.002279	0.000051	0.002652	0.000030
2.0	0.004084	0.000039	0.004811	0.000037	0.004637	0.000037

Table 3-2. Maximum differences between the obtained numerical results and known Blasius solution in the downstream locations for case - I

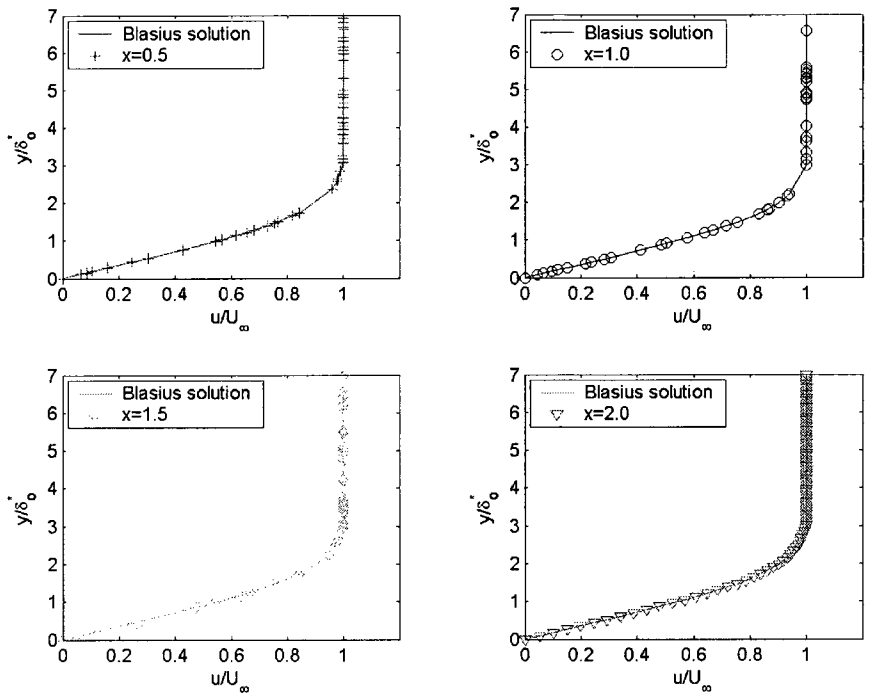

Figure 3-4 Similarity profiles of the stream-wise velocity component at downstream locations for case - II

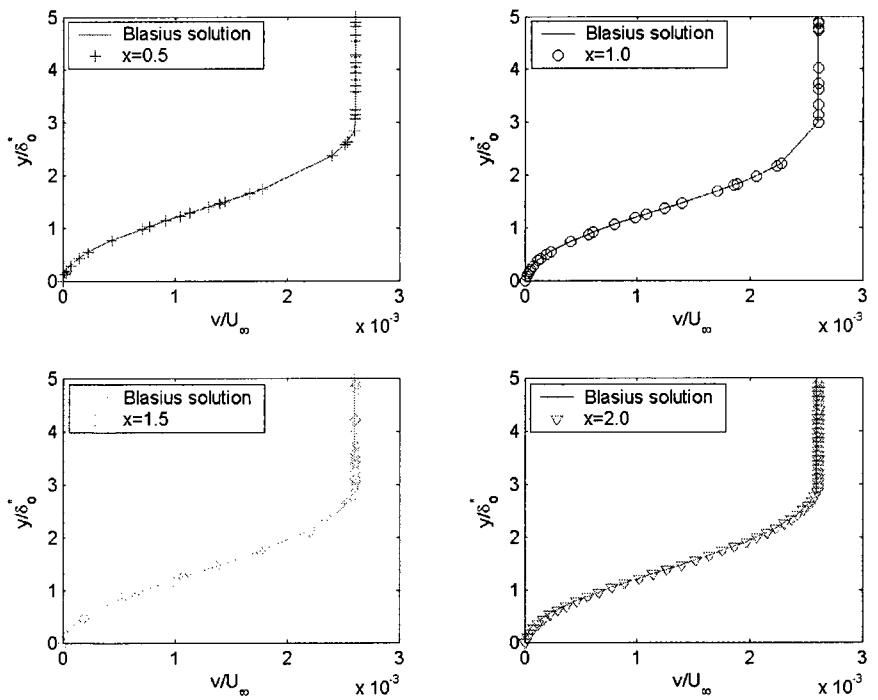

Figure 3-5 Similarity profiles of the wall-normal velocity component at downstream locations for case - II

Location	Velocity components (Maximum error)					
	Slip wall 1 (Z=0)		Mid plane (Z=0.5)		Slip wall 2 (Z=1)	
	u	v	u	v	u	v
0.5	0.002167	0.000012	0.001559	0.000012	0.002335	0.000012
1.0	0.002859	0.000020	0.000465	0.000020	0.002912	0.000019
1.5	0.003042	0.000026	0.001854	0.000021	0.003076	0.000026
2.0	0.005711	0.000031	0.005519	0.000032	0.005739	0.000032

Table 3-3. Maximum differences between the obtained numerical results and known Blasius solution in the downstream locations for case - II

As shown in the Figure 3-2 through Figure 3-5, our numerical data coincide well with the Blasius profiles at the downstream locations for both velocity components. At the same time, illustrated Table 3-2 and Table 3-3 also show that the maximum error between the known and the numerical results are comparably small at the chosen mid plane. Again, the tabulated values in the table at both side wall boundaries show that the enforced slip boundary conditions not refracted the flow significantly. This validation procedure shows the consistency of using these boundary and initial conditions in the spectral element method for the simulation of flat plate boundary layer.

Chapter 4

Initial Stage of Transition Process

The selection of appropriate boundary and initial conditions for the spectral element method is critical to simulate the initial stage of transition. The difficulties arise from the complicated nature of the non-linear system of partial differential equations. While selecting these boundary and initial conditions, care was taken that the stable method is not adversely affected. Therefore some boundary (i.e.: inflow and far-field) and initial conditions adopted in our numerical simulations are obtained from Fasel [05] which gives physically meaningful results with a relatively small integration domain to ensure that computational costs are kept within acceptable limits.

4.1 Boundary and Initial conditions of disturbances

Nowadays there are various analytical and numerical techniques available to introduce a disturbance into the boundary layer. An alternative form of disturbance forcing is to introduce a prescribed time-periodic function at the inflow or at the free stream boundary. For the present study the disturbance forcing is imposed at the inflow boundary. The emphasis of this study is to verify that the numerical techniques (i.e. spectral element method) used in the simulation is well suited to simulate the first stage of transition process via applying right boundary and initial conditions.

The inflow condition $\underline{u}_{in}$ is given by the time-periodic perturbation functions (u_p, v_p), which are only dependent on y and t, superimposed onto the Blasius profiles such that:

$$u_{in}(0,y,t) = u_B(o,y) + u_p(y,t) \tag{4-1}$$

$$v_{in}(0,y,t) = v_B(o,y) + v_p(y,t) \tag{4-2}$$

$$w_{in}(0,y,t) = 0 \tag{4-3}$$

where the perturbation functions u_p *and* v_p are sinusoidal in time (periodic) and written as:

$$u_p(y,t) = A^{\circ} u'_A(y)\cos(\beta t) \tag{4-4}$$

$$v_p(y,t) = A^{\circ} v'_A(y)\cos\left(\frac{\pi}{2} + \beta t\right) \tag{4-5}$$

The common amplitude factor A° allows experimentation with various perturbation amplitudes which are real and constant in time. For the present calculations, A° is chosen so that the absolute maximum value of u_p is 0.05% of the free stream velocity [05]. The so-called amplitude distributions $u'_A(y)$ and $v'_A(y)$ are taken from the numerical solutions of the Orr-Sommerfeld equation for time amplification which will be described in the following section 4.2. With these perturbation enforcement and other conditions, realistic Tollmien-Schlichting type disturbances are generated which propagate downstream and are amplified or damped in the downstream direction depending on the Reynolds number. This inflow condition is introduced in the code with the aid of Dirichlet boundary condition as explained in the previous Chapter 3.

At the upper boundary, perturbation velocity components decay asymptotically when approaching the far-field. If the far-field boundary is an insufficient distance from the flat plate, an erroneous disturbance arises throughout the computational domain. This erroneous disturbance occurs as a result of enforcing the far-field boundary conditions too close to the wall. This problem was overcome by the following conditions [05]:

$$\frac{\partial u'(x,y,t)}{\partial y} = -\alpha u'(x,y,t) \quad , \text{ at } y = Y \tag{4-6}$$

$$\frac{\partial v'(x,y,t)}{\partial y} = -\alpha v'(x,y,t) \quad , \text{ at } y = Y \tag{4-7}$$

where α is the wave number of the resulting perturbation flow (values for α can be obtained from corresponding linear stability theory calculations in section 4.2) and assumed that α is constant, although numerical results, as well as linear stability theory indicate that α varies with x. The prime denotes that the flow variables of the perturbation flow; they are defined as the difference between the total flow variables u, v and the corresponding variables of the undisturbed flow U, V :

$$u'(x,y,t) = u(x,y,t) - U(x,y) \tag{4-8}$$

$$v'(x,y,t) = v(x,y,t) - V(x,y) \tag{4-9}$$

As stated in the equations (4-6) and (4-7), perturbation velocity components decay slowly in the y direction. This allows a relatively small integration domain in the y direction and thus considerable savings in computer memory and computer time since it is not necessary to assume that u' *and* v' vanish on upper boundary. The boundary conditions (4-6) and (4-7) were derived by assuming neutral periodic behavior of the perturbation flow near this boundary. However, the use of this condition does not force strictly periodic behavior upon the flow. Damping or amplification of the disturbances was possible even on this boundary itself verified by Fasel [05].

Boundary conditions (4-6) and (4-7) are written in the weak formulation by multiplying a trial function v to employ in the spectral element method.

$$v\frac{\partial u'}{\partial y} = -\alpha v u' \tag{4-10}$$

$$v\frac{\partial v'}{\partial y} = -\alpha v v' \tag{4-11}$$

The above weak formulation is represented in the matrix form and perturbation velocities are written according to equations (4-8) and (4-9):

$$\begin{aligned} D_y(u-U) &= -\alpha M(u-U) \\ (D_y + \alpha M)u &= (D_y + \alpha M)U \end{aligned} \tag{4-12}$$

$$(D_y + \alpha M)v = (D_y + \alpha M)V \tag{4-13}$$

where D *and* M are surface derivative and mass matrices respectively. Right hand side terms of equations (4-12) and (4-13) are constructed as a forcing term and added in the right hand side of the Navier Stokes equation (2-42) at the upper boundary. As we know, the above boundary conditions are implicit therefore we need to solve for the total velocity u, v at the boundary itself. This lead us to add the surface matrix $(D_y + \alpha M)$ from the equations (4-12) and (4-13) with the volume Helmholtz matrix $\left(A/\mathrm{Re} + 3M/2\Delta t\right)$ in equation (2-42).

At the flat plate $y = 0$, the velocity components are zero.

$$\begin{aligned} u(x,o,t) &= 0 \\ v(x,0,t) &= 0 \\ w(x,0,t) &= 0 \end{aligned} \tag{4-14}$$

In the span-wise boundaries, 'arbitrary slip and no-penetration' boundary conditions are used where the span wise velocity components are zero at $z = 0$ and $z = Z$ which are enforced through Dirichlet boundary condition. However, many other authors employed

periodicity conditions for the span wise boundaries at $z = 0$ and $z = Z$ [31], [22], [06]. Thus, for all variables and their derivatives,

$$\begin{aligned} \underline{u}(x,y,0,t) &= \underline{u}(x,y,Z,t) \\ \left.\frac{\partial \underline{u}}{\partial z}\right|_{x,y,0,t} &= \left.\frac{\partial \underline{u}}{\partial z}\right|_{x,y,Z,t} \end{aligned} \tag{4-15}$$

In our spectral element scheme, difficulty of implementing periodicity condition in the span wise direction forced us to go for 'arbitrary slip and no-penetration' condition.

At the outflow boundary $x = X$, many conditions can be applied. These conditions have been the focus of study for the numerical simulation of flow transition by many researchers. In the present investigation, passive open boundary condition is applied as an outflow boundary condition:

$$\begin{aligned} \frac{\partial u}{\partial n} &= 0 \\ \frac{\partial v}{\partial n} &= 0 \\ \frac{\partial w}{\partial n} &= 0 \end{aligned} \tag{4-16}$$

This becomes in the weak formulation as:

$$\nu \frac{\partial \underline{u}}{\partial n} = 0 \tag{4-17}$$

This condition naturally exists in the weak formulation of the Navier-Stokes equation (2-18) as explained in the previous Chapter 3.

For the calculation of the unsteady disturbed flow field an initial condition is also required. Therefore initially at $t = 0$, undisturbed flow field U, V is assumed throughout the computational domain and then the disturbances are introduced ($t > 0$) during the

unsteady cycle of the computation. To obtain undisturbed flow field in spectral element method, we cannot get rid of unsteady terms in the Navier-Stokes equation as in other numerical schemes such as finite difference method because convection operator needs the previous time step solution as it was written in the explicit form [02]. Therefore we allow the complete Navier-Stokes equation to reach steady state with the boundary and initial conditions as stated in section 3.3 for validation procedure. Then we used this steady solution as initial condition to our problem of interest.

Now one may have a contradiction that instead of using the above steady state solutions, Blasius solution could be used in the entire flow field as initial condition. Indeed, the steady state solutions closely agree with the Blasius solution as shown in the Figure 3-2, so that plotted profiles coincide in each down stream locations. In our present work, the reactions of the flow to very small disturbances are investigated. Therefore the use of the Blasius solution could initially makes disturbances and thus distorts the transient behavior of the flow field. This led to use steady state solution where the unwanted initial distortion in the transient flow can be eliminated [05].

4.2 Linear stability

The remarkable process of transition is investigated theoretically based on the assumption that laminar flows are affected by certain small disturbances. In the case of a boundary layer on a solid body placed in a stream these disturbances may originate in the inlet or due to the wall roughness or to irregularities in the external flow. The theory attempts to follow up in time the behavior of such disturbances when they are superimposed on the main flow. The behavior of these disturbances can increase or die out with time. If the

disturbances decay with time, the main flow is considered stable. On the other hand, if the disturbances increase with time the flow is considered unstable, and there exists the possibility of transition to a turbulent flow.

The theory of stability of laminar flows decomposes the motion into a basic flow and a disturbance superimposed on it. An assumption is made that the quantities related to the disturbances are very small compared with the corresponding quantities of the main flow. The investigation of the stability of such a disturbed flow can be carried out with the aid of the equations of motion and analyzes the manner in which they develop in the flow. We restrict our attention to the case of two-dimensional, incompressible, viscous, Newtonian basic flow and an equally two-dimensional small disturbance. Parallel flow is assumed as a basic flow in the boundary layer, and then the stream-wise mean velocity U depends only on y coordinate. As far as the main flow is concerned, it is obviously necessary to assume the pressure. Thus we assume a basic flow with

$$U(y),\ V=0,\ P(x,y) \tag{4-18}$$

Then the basic flow is superimposed with a two-dimensional disturbance and the resultant motion is described by:

$$\begin{aligned} u &= U(y)+u'(x,y,t) \\ v &= v'(x,y,t) \\ p &= P(x,y)+p'(x,y,t) \end{aligned} \tag{4-19}$$

where u' *and* v' are the components of disturbance velocity. Substituting equations (4-19) into the two dimensional incompressible Navier-Stokes equation, and neglecting quadratic terms with respect to the linear terms, and considered that the basic flow itself satisfies the Navier-Stokes equations, we obtain the linearized version of the Navier-

Stokes equation in which the only contributions from the basic flow is associated with U and dU/dy such that:

$$\frac{\partial u'}{\partial t}+U\frac{\partial u'}{\partial x}+v'\frac{dU}{dy}+\frac{1}{\rho}\frac{\partial p'}{\partial x}=\upsilon\left(\frac{\partial^2 u'}{\partial x^2}+\frac{\partial^2 u'}{\partial y^2}\right) \tag{4-20}$$

$$\frac{\partial v'}{\partial t}+U\frac{\partial v'}{\partial x}+\frac{1}{\rho}\frac{\partial p'}{\partial y}=\upsilon\left(\frac{\partial^2 v'}{\partial x^2}+\frac{\partial^2 v'}{\partial y^2}\right) \tag{4-21}$$

$$\frac{\partial u'}{\partial x}+\frac{\partial v'}{\partial y}=0 \tag{4-22}$$

The above equations are the fundamental hydrodynamic equations for small disturbances. From the above basic equations (4-20) and (4-21), the pressure terms are eliminated by differentiating equations (4-20) and (4-21) with respect to y and x correspondingly, and subtracting the second from the first. The resulting equation is a linear and homogeneous in u' and v' :

$$\begin{aligned}&\frac{\partial^2 u'}{\partial y\partial t}+U\frac{\partial^2 u'}{\partial x\partial y}+\frac{\partial U}{\partial y}\frac{\partial u'}{\partial x}+\upsilon\frac{\partial^2 U}{\partial y^2}+\frac{\partial v'}{\partial y}\frac{\partial U}{\partial y}-\frac{\partial^2 v'}{\partial x\partial t}-\frac{U\partial^2 v'}{\partial x^2}=\\&\upsilon\left(\frac{\partial^3 u'}{\partial x^2\partial y}+\frac{\partial^3 u'}{\partial y^3}-\frac{\partial^3 v'}{\partial x^3}-\frac{\partial^3 v'}{\partial y^2\partial x}\right)\end{aligned} \tag{4-23}$$

As it has already been assumed that the perturbation is two-dimensional, it is possible to introduce a stream function $\psi(x,y,t)$ by integrating the equation of continuity (4-22). The stream function, which has the exponential structure, allows the solution to oscillate and grow/decay in space and time, depending on the real and imaginary parts of α and β :

$$\psi(x,y,t)=\varphi(y)e^{i(\alpha x-\beta t)}=\varphi(y)e^{i\alpha(x-ct)} \tag{4-24}$$

where $\varphi(y)$ represents the initial amplitude of the stream function, the stream wise wave number of the disturbance is given by $\alpha = 2\pi/\lambda$ here λ is the wave length, and t is the time. Since β and hence c are generally complex quantities, equations (4-24) may be written as:

$$\psi(x,y,t) = \varphi(y)e^{i(\alpha x-(\beta_r+i\beta_i)t)} = \varphi(y)e^{i\alpha(x-(c_r+ic_i)t)} \tag{4-25}$$

where β_r, the real part of β,is the circular frequency of the partial oscillation; β_i, the imaginary part of β, is the coefficient of amplification or damping, depending on whether it is positive or negative; and $c_r = \beta_r/\alpha$ is the velocity of propagation of the wave in the x direction (phase velocity) and c_i again determines the degree of amplification or damping. The amplitude function φ of the fluctuation is assumed to depend only on y coordinate because the mean flow depends only on y. It is possible to obtain perturbation velocity components from equation (4-24) which has the wave like solution:

$$u' = \frac{\partial\psi}{\partial y} = \varphi'(y)e^{i(\alpha x-\beta t)} \tag{4-26}$$

$$v' = -\frac{\partial\psi}{\partial x} = -i\alpha\varphi(y)e^{i(\alpha x-\beta t)} \tag{4-27}$$

Introducing these u' and v' into the equation (4-23) we obtain the following fourth order ordinary differential equation for the amplitude function $\varphi(y)$:

$$(U-c)(\varphi''-\alpha^2\varphi)-U''\varphi = -\frac{i}{\alpha\,\mathrm{Re}}(\varphi''''-2\alpha^2\varphi''+\alpha^4\varphi) \tag{4-28}$$

where the primes represent differentiation with respect to dimensionless y coordinate. This is the linear stability equation commonly referred as the Orr-Sommerfeld equation.

A parallel, undisturbed mean laminar flow that solves the Navier-Stokes equations can become unstable if certain conditions on the flow are satisfied, and this Orr-Sommerfeld equation determines precisely what these conditions are [58]. The above equation (4-28) is written in the non-dimensional form by measuring velocities according to a scale set by the free stream velocity of the basic flow, and by measuring lengths according to the boundary layer displacement thickness, and Re denotes the Reynolds number based on the displacement thickness.

Now we are in a position to specify boundary conditions. For the boundary layer flow, relevant boundary conditions are 'no-slip and no-penetration' at the solid wall. According to the linear stability theory, the perturbation velocities vanish far out in the main stream, so we assume velocity components are zero at far-field. Thus:

$$\begin{aligned} &y = 0 : u' = v' = 0, \varphi = 0, \varphi' = 0; \\ &y \to \infty : u' = v' \to 0, \varphi \to 0, \varphi' \to 0; \end{aligned} \tag{4-29}$$

The Orr-Sommerfeld equation (4-28) can be written in the matrix form as:

$$(U - c)(D^2 - \alpha^2)\varphi - U''\varphi = -\frac{i}{\alpha \,\mathrm{Re}}(D^4 - 2\alpha^2 D^2 + \alpha^4)\varphi \tag{4-30}$$

where D is a derivative matrix using Chebychev collocation method [59]. The computer program is sufficiently general to allow a variety of velocity profiles to be studied. It is well known that the solution of equation (4-30) with the boundary conditions (4-29) poses an eigen value problem such that:

$$\underbrace{\left[\tfrac{1}{\mathrm{Re}}(D^4 - 2\alpha^2 D^2 + \alpha^4) + i\alpha U'' - i\alpha U(D^2 - \alpha^2)\right]}_{A}\varphi = c\underbrace{\left[-i\alpha(D^2 - \alpha^2)\right]}_{B}\varphi \tag{4-31}$$

$$A\varphi = cB\varphi$$

In the spatial analysis we would get a non-linear (quadratic) eigen value problem, here it is assumed that U, β and Re are real and given, and the problem is that of finding a complex eigen value α with a corresponding eigen vector φ, one assumes that the solution only oscillates in time at a given spatial position, but is allowed to grow/decay and oscillate in space. In the temporal analysis, the corresponding problem is that of finding a complex eigenvalue $c = c_r + ic_i$ for given real values of U, Re and α where the solution grows/decay and oscillates in time but only oscillate in space. In particular present method is concerned by verifying Gaster's equations [10]; it is convenient to adopt his notation to distinguish between the cases of time amplification (T) and space amplification (S). Thus:

Case (T); time dependent, $\alpha_i(T) = 0$

$$\alpha = \alpha_r(T), \beta = \beta_r(T) + i\beta_i(T) \tag{4-32}$$

Case (S); spatially dependent, $\beta_i(S) = 0$

$$\alpha = \alpha_r(S) + i\alpha_i(S), \beta = \beta_r(S) \tag{4-33}$$

Therefore the relation between space and time amplification can be represented by Gaster's equations:

$$\alpha_r(T) = \alpha_r(S) \ , \ \beta_r(T) = \beta_r(S) \tag{4-34}$$

This relationship was again proofed by Jordinson [21] in his PhD thesis. This was used to verify our results with other authors.

In the present work, we considered the temporal setting where the problem formulation can be cast into the linear form $A\varphi = cB\varphi$ that is the classical eigenvalue problem to seek

complex eigenvalues of $c = c_r + ic_i$. We take into account only the least stable eigen mode from the spectrum of eigen values. Here c_r represents the phase velocity of the prescribed disturbance whereas the sign of c_i determines whether the wave is amplified $(c_i > 0)$ or damped $(c_i < 0)$. Therefore we have stability for the corresponding flow (U, Re) if all $c_i < 0$, main flow has instability and the small perturbation introduced to the system is amplified in time for the given value of α if there exist a $c_i > 0$ and the neutral stability if at least one $c_i = 0$, the remaining c_i having vanishing or negative imaginary parts. All these calculations are performed by using the standard eigen value software MATLAB [59].

Generally the stability analysis of the flow field in a boundary layer is more difficult than the other problem of interests. This is due to the fact that one of the boundary condition for boundary layer flow is at infinity. Secondly, the velocity profile $U(y)$ of the main flow in a boundary layer is not an exact solution of the Navier-Stokes equation. Finally the Orr-Sommerfeld equation itself was derived on the assumption that the main flow $U(y)$ does not change in the direction of the main stream. These assumptions are really not satisfied in the boundary layer flow. All these situations make the stability analysis of a boundary layer flow more difficult than other flows.

In the present work, the flow in the boundary layer is assumed to be given by the Blasius solution. This solution can be expressed in dimensional form as:

$$\begin{aligned} U &= U_\infty f'(\eta) \\ V &= \sqrt{\frac{\upsilon U_\infty}{2x}}(\eta f' - f) \end{aligned} \tag{4-35}$$

where η is defined by the relation $\eta = y\sqrt{U_\infty/2\upsilon x}$. Thus, the mean flow is evidently non-parallel. However, the ratio V/U is given by:

$$V/U = \sqrt{\upsilon/2U_\infty x}\left(\eta - f/f'\right) = G(\eta)/\mathrm{Re}^* \tag{4-36}$$

where Re^* is the Reynolds number based on displacement thickness. Hence, V/U and $\partial U/\partial x$ are approximately given by $O\left(1/\mathrm{Re}^*\right)$. Therefore the mean flow in the boundary layer may be treated as parallel [21].

To solve the generalized eigenvalue problem, we need to know the mean flow U and its second derivative d^2U/dy^2. This mean flow and its derivatives are obtained by using Newton's divided difference interpolating polynomials which are used to interpolate the Blasius profile [30]. Here four data points are connected with a third order polynomial such that:

$$f_3(x) = b_0 + b_1(x - x_0) + b_2(x - x_0)(x - x_1) + b_3(x - x_0)(x - x_1)(x - x_2) \tag{4-37}$$

where the coefficients are given by $b_0 = f(x_0)$, $b_1 = f[x_1, x_0], b_2 = f[x_2, x_1, x_0]$ and $b_3 = f[x_3, x_2, x_1, x_0]$. Here the bracket [] function evaluations are finite divided differences which are given by the n^{th} finite divided difference:

$$f[x_n, x_{n-1}, \ldots, x_0] = \frac{f[x_n, \ldots, x_1] - f[x_{n-1}, \ldots, x_0]}{x_n - x_0} \tag{4-38}$$

The interpolated velocity profiles are shown in Figure 4-1. The profiles at different stations along the flat plate are similar which means that they can be made to coincide

when they are plotted against y/δ^*. Here δ^* denotes the boundary layer displacement thickness which has been shown by $\delta^* = 1.7208\sqrt{\upsilon x/U_\infty}$.

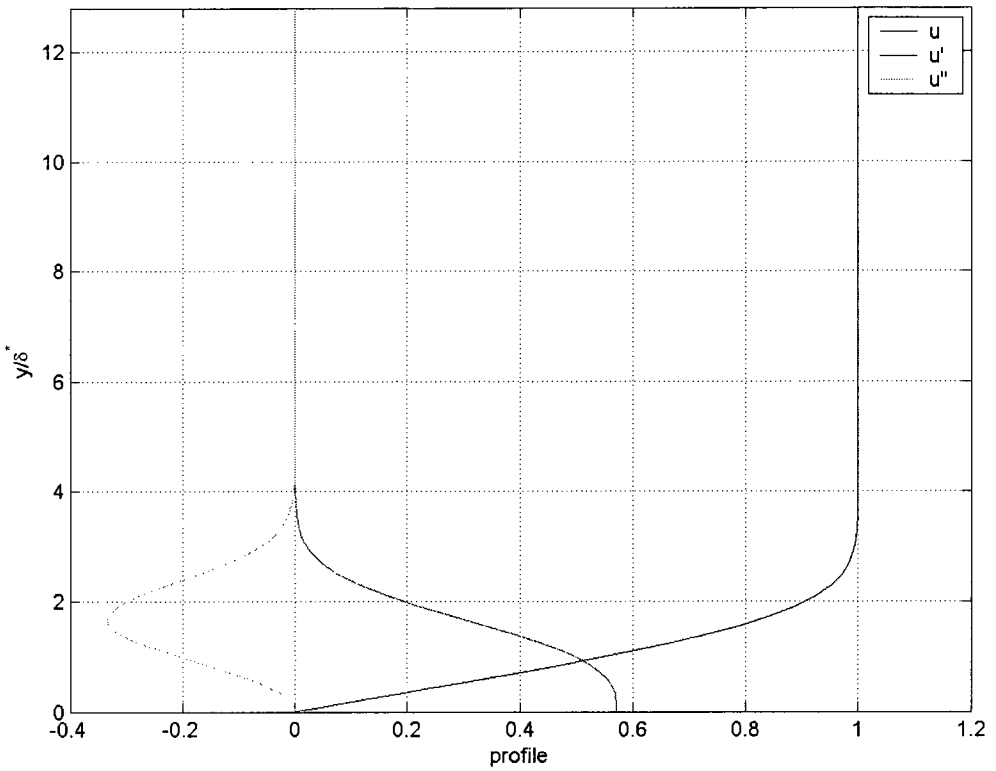

Figure 4-1 Velocity distribution and its derivatives in the boundary layer

The results of the numerical investigations obviously depend on the value of the step size used in the calculations. The number of points (n) used in the collocation method is related to the step length h which is given by $h = Y/n$. Here the numerator of the fraction Y is chosen as an integral multiple of the displacement thickness δ^*, and where $y = Y$ is the point in the mainstream at which the outer boundary condition is applied. Changing the number of points (n), affect the results remarkably shown by Jordinson in his PhD thesis [21]. In our calculations, we have taken n=80 to compare our results with other authors [43],[28],[21].

The above prescribed boundary layer flow $U(y)$ can be represented graphically in a $\alpha^* - \mathrm{Re}^*$ diagram. Each point of this diagram corresponds to a pair of values (c_r, c_i). In particular, the locus $c_i = 0$ separates the region of stable from that of unstable disturbances. This locus is called the curve of neutral stability.

Obtained stability curves are shown in Figure 4-2. The region inside the neutral curve ($c_i = 0$) is unstable and that outside the curve is stable, while the curves themselves represent neutral disturbance waves. One sees that at low Reynolds number, all waves are stable.

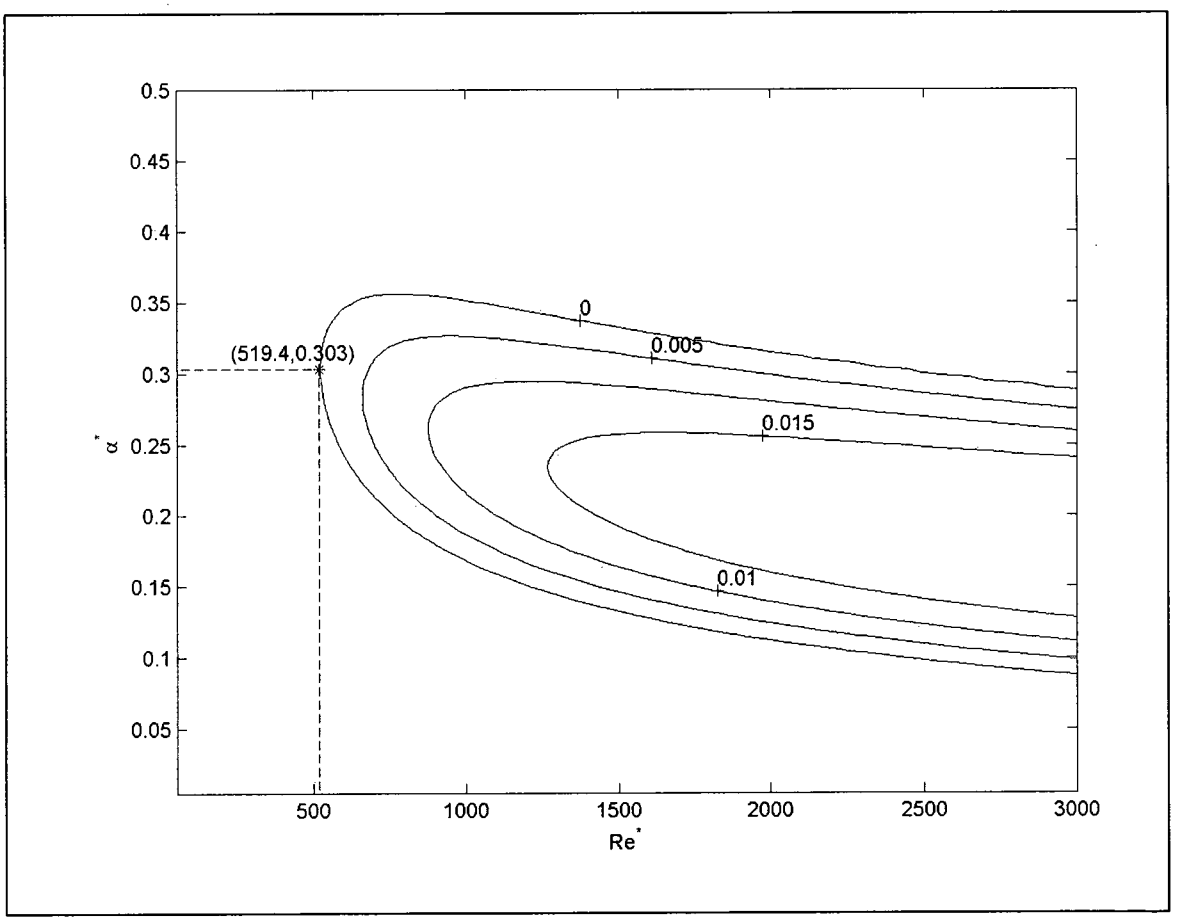

Figure 4-2 Thumb curves of constant c_i for the two dimensional flat plate boundary layer.

The point on this curve, at which the first appearance of an unstable wave, is called the critical Reynolds number with respect to the type of laminar flow under consideration. This instability is known as the Tollmien-Schlichting instability and is given by:

$$\mathrm{Re}_{crit} = \frac{U_\infty \delta^*}{\upsilon} = 519.4 \qquad (4\text{-}39)$$

The corresponding value of wave number α is 0.303. Analogous values for the critical Reynolds number based on analytical methods are 425 (Shen), 475 (Schlichting) and 330 (Timman and Zaat) [49],[45],[46],[55]. This can be partly demonstrated by considering the critical Reynolds numbers of numerical solutions are – 530 (Kurtz), 515 (Kaplan), 520 (Osborne) and 522 (Craven) [28],[29],[23],[43]. Figure 4-2 is compared with the neutral stability curve of Hoepffner [18] where also the same collocation method is used. The two curves appear to be identical, and have approximately the same critical Reynolds number. In view of this consistency it seems reasonable to regard our results with some confidence. This is the point of instability for the boundary layer on a flat plate where exists the smallest unstable wave length. Just as a lower limit exists for a Reynolds number, there is an upper limit for the characteristic magnitudes of the disturbances beyond which no further instabilities occur. If there is a small amount of free-stream disturbance in the flow upstream of the flat plate, all the perturbations introduced in the boundary layer close to the plate would decay in amplitude, until they reach the downstream location of the critical Reynolds number. At this point onward, the perturbations corresponding to the unstable waves will grow exponentially.

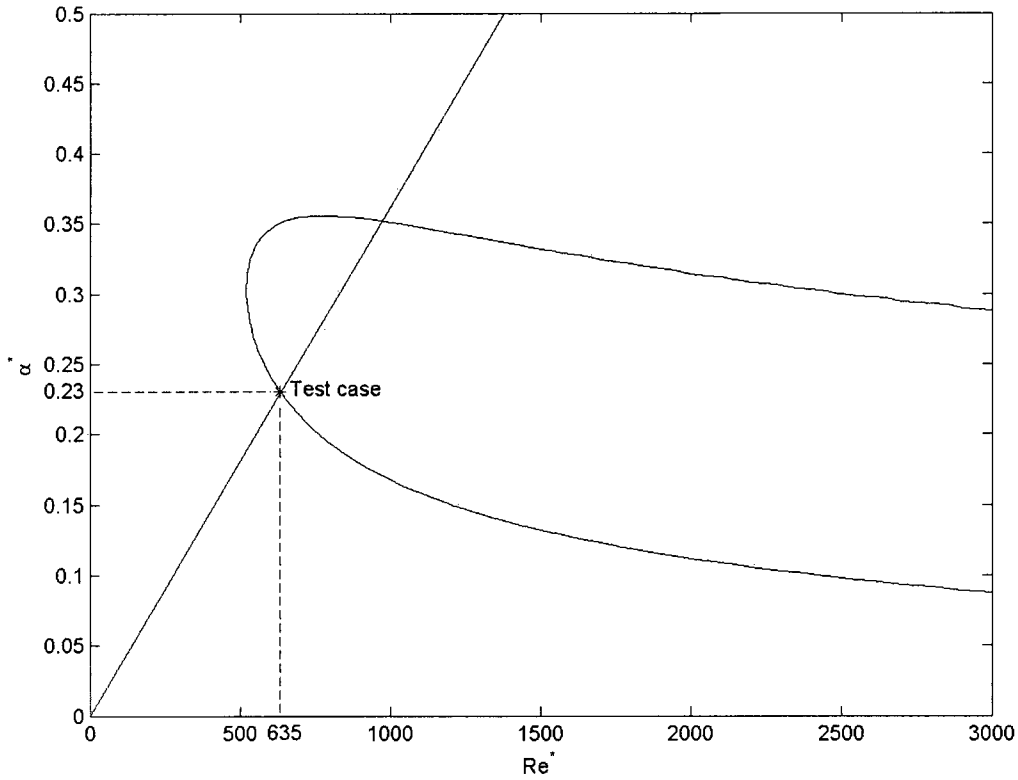

Figure 4-3. A test case on the stability diagram of linear stability theory.

In Figure 4-3, dimensionless disturbance wave number $\alpha^* = \alpha\delta^*$ versus Reynolds number $\mathrm{Re}^* = {U_\infty \delta^*}/{\upsilon}$ are plotted. An assumption is made that the dimensional disturbance wave number α or a dimensionless wave number parameter $W = {\alpha^*}/{\mathrm{Re}^*}$ is constant on rays through origin. The conditions of the perturbation flow for various downstream locations are obtained from the corresponding points on the ray moving away from the origin. For example at a constant wave number parameter ($W * 10^4 = 3.62$), the disturbance begins to grow at $\mathrm{Re}^* \approx 635$ on the lower branch of the stability loop.

The above test case is compared with the benchmark results of Fasel [05]. The spectrum of eigenvalues of the Orr-Sommerfeld equation for boundary layer flow is addressed in

Figure 4-4 for the test case $\mathrm{Re} = 635$ and $\alpha = 0.230$. This case lies at the neutral stability curve and the eigen value corresponding to this mode is given by $c_r = 0.366820, \mathrm{c_i} = 0$ which agreed well with the results of Jordinson [20]. In general, the spectrum of the equation is continuous and discrete for unbounded flows such as boundary-layer flow [19] . We restricted the display to those eigen values with $c_i \geq -1$, since the disturbances corresponding to eigen values with large negative imaginary parts are of little interest.

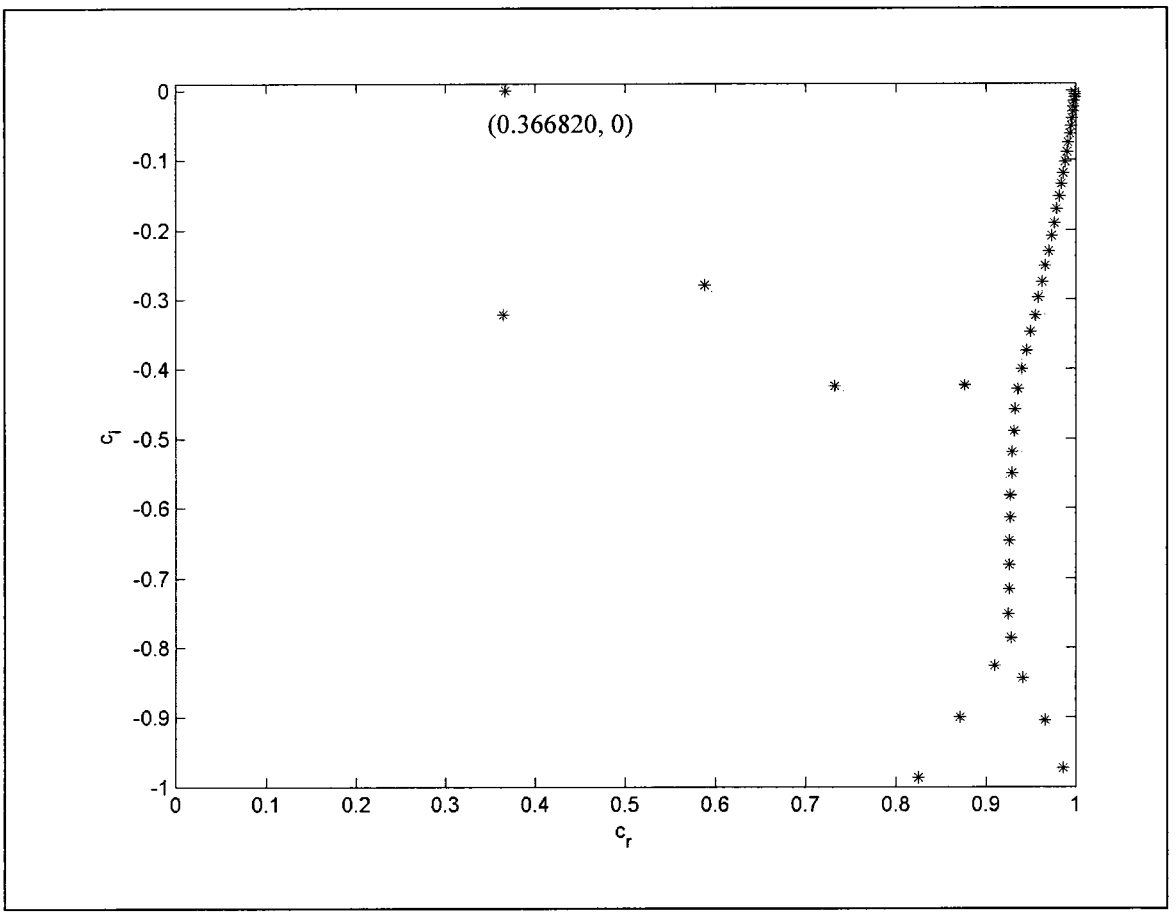

Figure 4-4 The Spectrum of the Orr-Sommerfeld equation for flat plate boundary layer flow.

Perturbation velocities from equations (4-26) and (4-27) are rearranged to obtain perturbation profiles which are required in the above section 4.1:

$$u' = \varphi'(y)\left[\cos(\alpha x - \beta t) + i\sin(\alpha x - \beta t)\right] \tag{4-40}$$

$$\begin{aligned} v' &= -i\alpha\varphi(y)[\cos(\alpha x - \beta t) + i\sin(\alpha x - \beta t)] \\ &= \alpha\varphi(y)[\sin(\alpha x - \beta t) - i\cos(\alpha x - \beta t)] \end{aligned} \tag{4-41}$$

Real terms are considered to obtain u_r' *and* v_r' such that:

$$u_r' = \varphi'(y)\cos(\alpha x - \beta t) = u_A'(y)\cos(\alpha x - \beta t) \tag{4-42}$$

$$v_r' = \alpha\varphi(y)\sin(\alpha x - \beta t) = v_A'(y)\cos\left(\alpha x + \pi/2 + \beta t\right) \tag{4-43}$$

Here $u_A'(y), v_A'(y)$ are amplitude distributions or perturbation profiles which are obtained from the numerical solutions of the Orr-Sommerfeld equation by using collocation method as explained above [59]. The perturbation profiles used in the above test case are shown in Figure 4-5, which are normalized by setting $\max|u_A'(y)| = 1$.

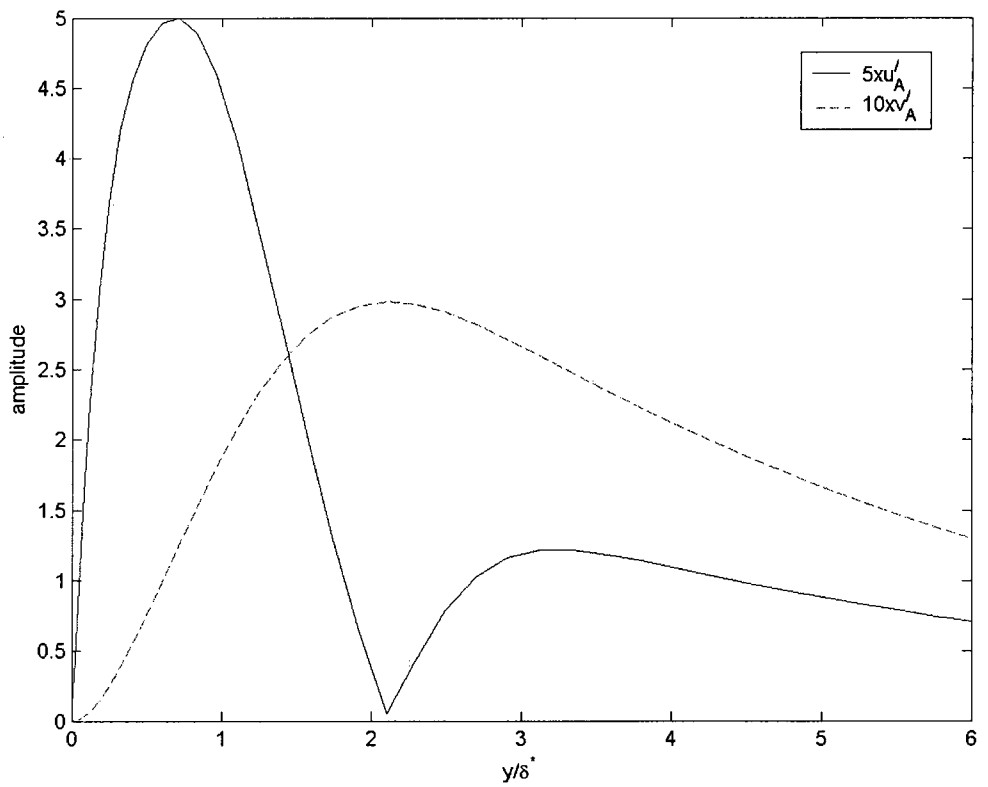

Figure 4-5 Perturbation profiles (amplitude distributions) for $W = 3.62, \mathrm{Re}^* = 635$.

4.3 Computational Results

To get better insight into the flow physics of the initial stage of transition and a better understanding of the numerical scheme, results from the spectral element methods are compared with theory, experiments and related studies from other authors. Figure 4-6 shows a generic flow sequence of settings in the modal-SEM model to analyze our problem of interest.

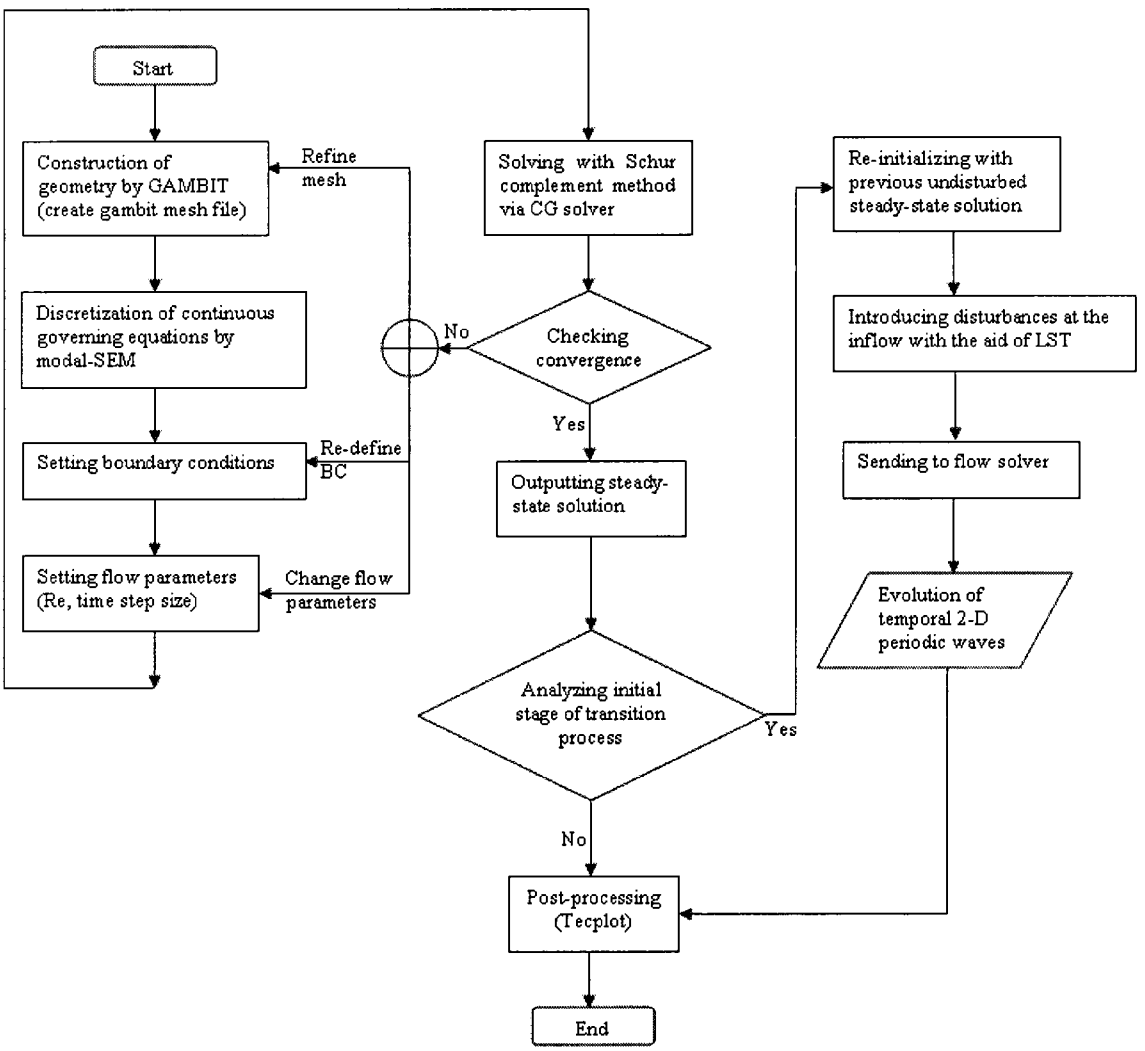

Figure 4-6.Flow chart to analyze the initial stage of transition process

To study the initial stage of transition over a flat plate, this thesis presents a test case and several other simulation cases for Gambit generated tetrahedral elements. The flow domain is displayed in Figure 4-7. Computations are carried out with different grid sizes.

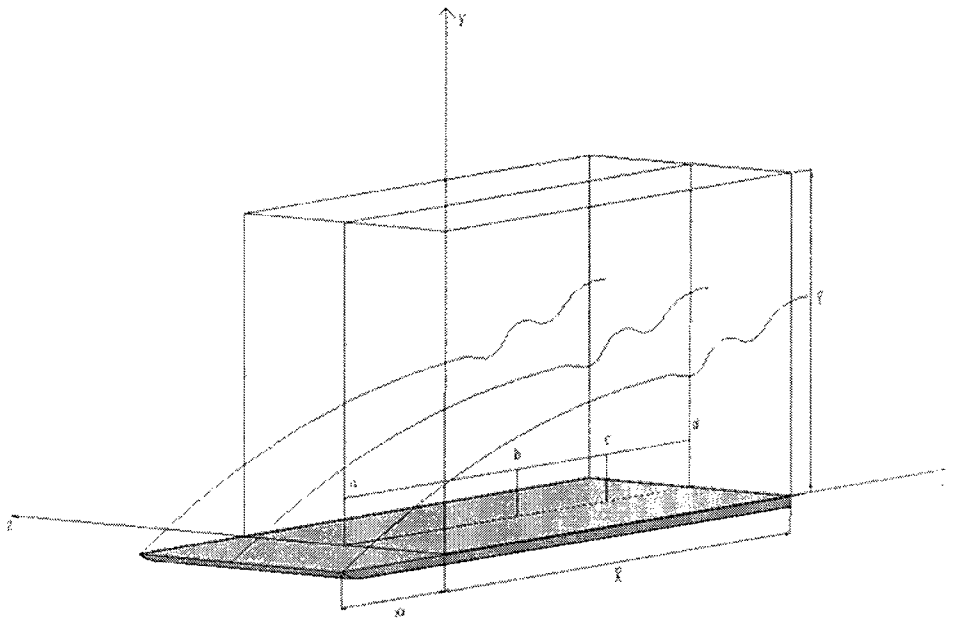

Figure 4-7. Integration domain.

The flow parameters used throughout this work are listed in the Table 4-1. The reference values for Reynolds number are based on the inlet displacement thickness and the free-stream velocity.

U_∞	$30 m/s$
ρ	$1 kg/m^3$
μ	$1.5x10^{-5} m^2/s$

Table 4-1. Flow parameters

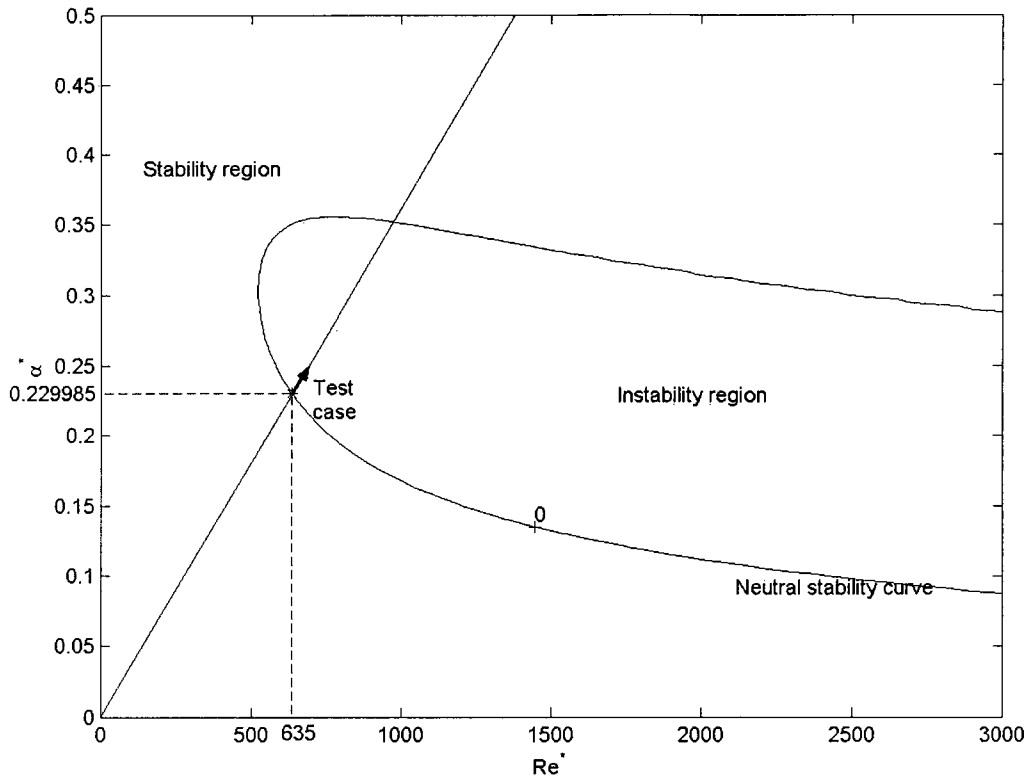

Figure 4-8. A test case on the stability diagram of linear stability theory obtained from numerical solution of the Orr-Sommerfeld equation for the case of temporal amplification.

To demonstrate the suitability of the numerical method for the investigation of the initial stage of transition, primarily a test case ran as shown in Figure 4-8 where a ray has been drawn through the origin. The perturbation conditions are applied at the inlet which corresponds to the point (635, 0.22985) on the lower branch of the neutral stability curve. Downstream locations of the disturbed flow correspond to points on the ray away from the origin. As explained in the previous section, disturbances should be amplified at downstream locations corresponding to points inside the instability region and damped at locations corresponding to points in the stability region. When proceeding in the downstream direction for our test case, instability region is entered therefore disturbances

should grow at downstream locations. The parameters used in the test case calculations are listed in Table 4-2.

Re^*	635	
α^* (wave number)	0.229985	
β^* (frequency)	0.084363	
Δx	0.250	
Δy	0.423	
Δz	0.250	
Δt	$P = 2$	0.020
	$P = 3$	0.010

Table 4-2.test case parameters

Temporal evolutions of the velocity components are plotted at different downstream locations in Figure 4-11 to Figure 4-14 for the same mesh size with different polynomial orders 2 and 3 and observed the flow behavior with the Figure 4-9 and Figure 4-10 obtained from Fasel [05].

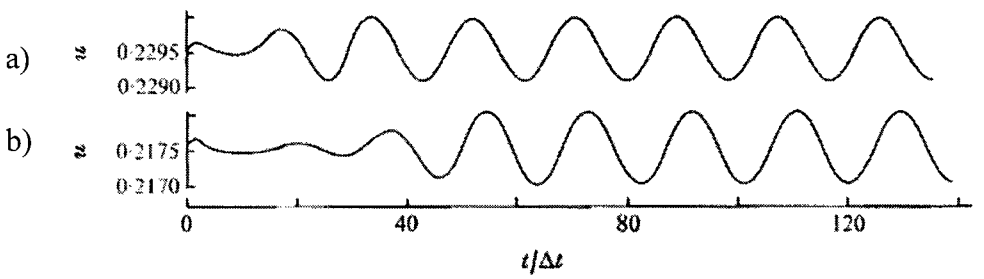

Figure 4-9. Test case results of velocity component u obtained from Fasel [05] for two different downstream locations where the top figure-'a' is near to upstream boundary.

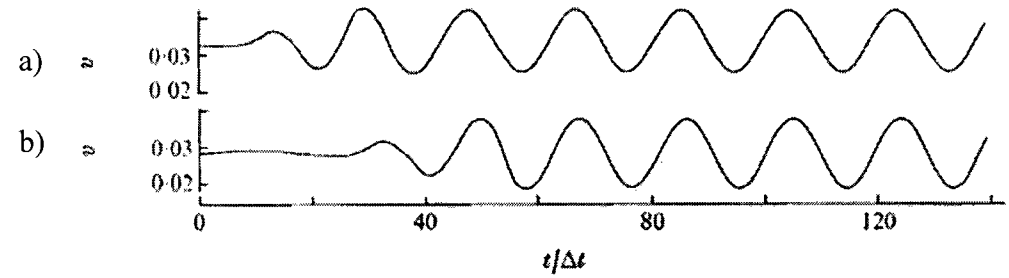

Figure 4-10. Test case results for velocity component v obtained from Fasel [05] for two different downstream locations where the top figure-'a' is near to upstream boundary.

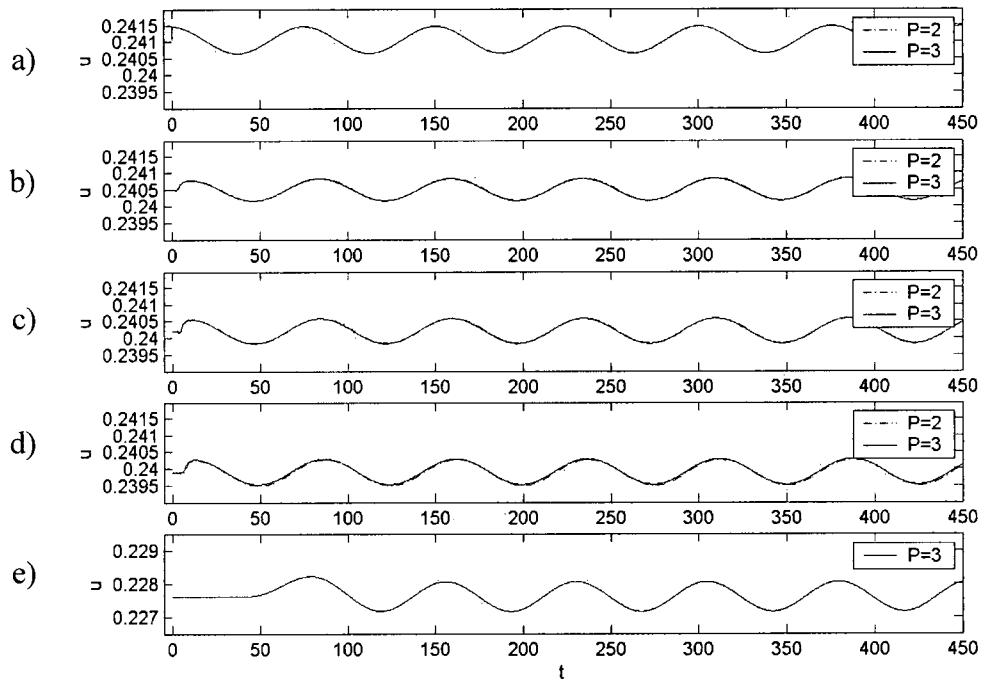

Figure 4-11. Temporal developments of u for the disturbed flow test case at y=0.423 and various downstream locations, reading from top to bottom $x = 0,1,1.5,2,21.5$ as shown in Figure 4-7.

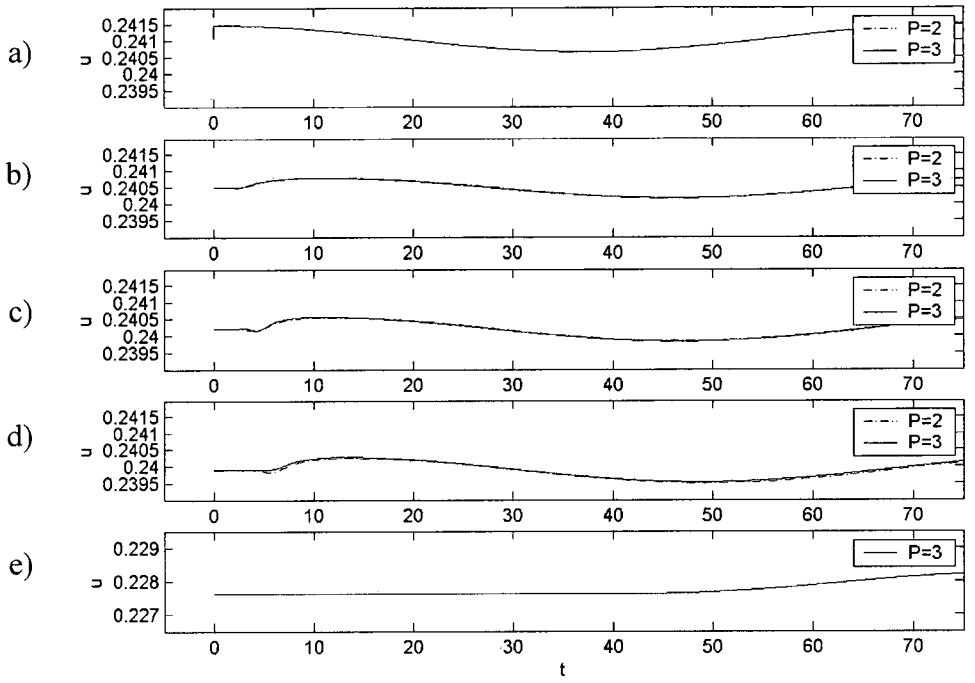

Figure 4-12. Zoomed view of Figure 4-11.

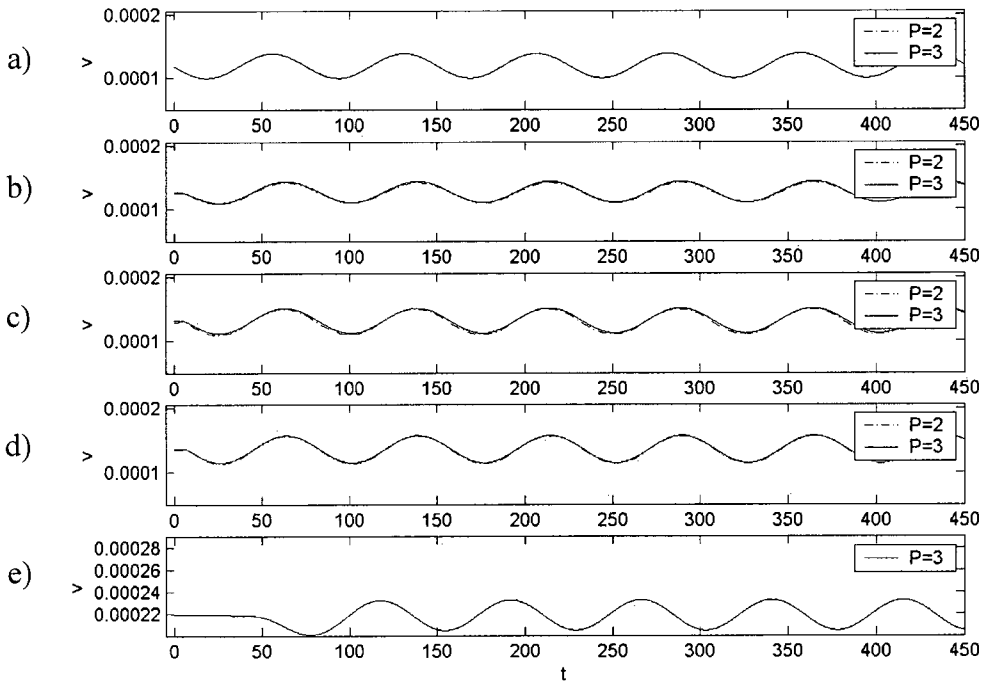

Figure 4-13. Temporal developments of v for the test case at y=0.423 and various downstream locations, reading from top to bottom $x = 0, 1, 1.5, 2, 21.5$ as shown in Figure 4-7.

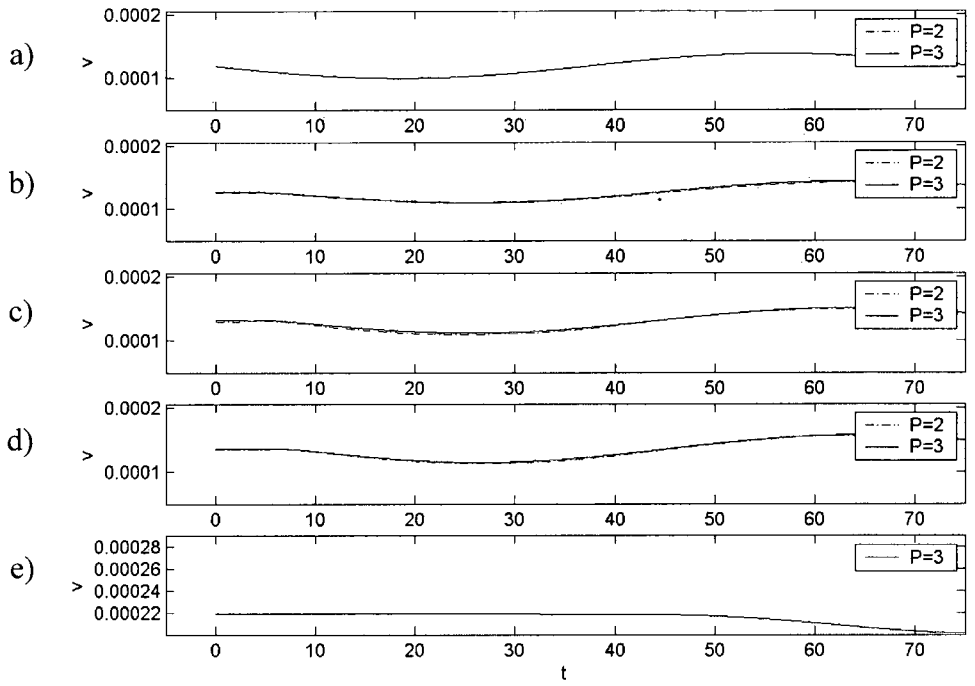

Figure 4-14. Zoomed view of Figure 4-13.

Fasel used the Navier-Stokes equation in vorticity-transport form to simulate the flow by finite-difference scheme. To ensure same order of magnitude of both coordinates and both velocity components in the numerical operations, he stretched the y-coordinate and the wall normal velocity component- v by a factor $\sqrt{\mathrm{Re}}$. At the same time, the parameters he used to write the variables in non-dimensional form are different from ours. The visualization of the Figure 4-11 and Figure 4-13 are comparably similar to Fasel results and the behavior of the flow clearly shows the temporal development of the disturbed flow in the downstream direction and the propagation of the time-wise sinusoidal disturbances which are introduced at the upstream boundary. Different downstream locations are considered as shown in the Figure 4-7 including inlet boundary to plot each flow variables u, v against time at a constant distance y normal to the flat plate. Both polynomial orders 2 and 3 gives similar results as seen in the Figure 4-11 and Figure

4-13. The Figure 4-11e and Figure 4-13e are plotted at identical downstream location as Fasel and the behavior of the flow fairly agreed with the Figure 4-9a and Figure 4-10b where minor deviations occurred due to the used scheme and the neglected terms in the governing equations. From the observation we can say that after some time has left the flow behavior is apparently of a periodic nature which is first reached near the upstream boundary and last near the downstream boundary. In the downstream locations, the amplitudes of the waves are tabulated in Table 4-3 for polynomial orders 2 and 3.

Location	u velocity amplitude			v velocity amplitude		
Polynomial order	P=2	P=3	Fasel results	P=2	P=3	Fasel results
b, x=01.0	0.0006686	0.0006511	-	0.00003105	0.00003316	-
c, x=01.5	0.0007380	0.0007448	-	0.00004003	0.00003941	-
d, x=02.0	0.0007691	0.0007633	-	0.00004316	0.00004257	-
e, x=21.5	-	0.0008984	≈0.0008823	-	0.00002770	≈0.0000502

Table 4-3.Wave amplitudes in the downstream locations for the order 2 and 3

As illustrated in Table 4-3, when the flow moves into the unstable region b, c, d and e (location-a is not taking into consideration where the amplitude value is supplied at the inlet through Dirichlet boundary condition), amplification of the waves are noted which justify the argument that the beginning of transition takes place through wave amplification in the downstream direction. The wave amplitudes obtained at downstream location-e complies with the Fasel results for velocity component-u but the wall normal component-v shows big difference. However, the variation of resultant velocity wave amplitude is less than 2%. A further increase in the size of amplified waves can be observed by taking a location very far from the upstream boundary if longer domain is used. The domain used herein is small to save computational cost. A longer domain will

be too expensive because of longer processing time to achieve statistically stationary results and huge memory requirement.

According to the linear stability theory, flow variables u and v can be written as:

$$\begin{aligned} u &= U_B(y) + u'(y,t) = U_B + \varphi'(y)e^{i(\alpha x - \beta t)} \\ v &= V_B(y) + v'(y,t) = V_B - i\alpha\varphi(y)e^{i(\alpha x - \beta t)} \end{aligned} \tag{4-44}$$

where φ and φ' are complex variables. At the same time α and β are also complex numbers depends on the setting (temporal or spatial) of the linear stability theory.

In temporal setting-

$$\begin{aligned} u &= U_B + e^{\beta_i t}\left(\varphi_r' + i\varphi_i'\right)e^{i(\alpha x - \beta_r t)} \\ v &= V_B - i\alpha e^{\beta_i t}\left(\varphi_r + i\varphi_i\right)e^{i(\alpha x - \beta_r t)} \end{aligned} \tag{4-45}$$

In spatial setting-

$$\begin{aligned} u &= U_B + e^{-\alpha_i x}\left(\varphi_r' + i\varphi_i'\right)e^{i(\alpha_r x - \beta t)} \\ v &= V_B - ie^{-\alpha_i x}\left(\alpha_r + i\alpha_i\right)\left(\varphi_r + i\varphi_i\right)e^{i(\alpha_r x - \beta t)} \end{aligned} \tag{4-46}$$

The results from the temporal development of the disturbed flow are not capable to compare with the analytical results of the linear stability theory because as seen in the equation (4.45), both velocity components amplitude varies with time. However the spatial development of the disturbed flow can be compared with the spatial setting of linear stability theory results obtain from equation (4.46) but in the current study our interest is limited to the analysis of temporal development.

For a more quantitative comparison with linear stability theory, enormous amount of simulation cases can be analyzed with the aid of the stability diagram. In the present investigation, we considered few more simulation cases by varying Reynolds number, wave number and frequency of the wave for different grid sizes.

Three simulation cases are chosen to discuss here in more detail. They are shown in Figure 4-15 which is a stability diagram of linear stability theory obtained from the numerical solution of the Orr-Sommerfeld equation for the case of temporal disturbance amplification. For case-1 and case-3, locations of the upstream boundary correspond to points on the lower branch of the neutral stability curve but for case 2 calculation starts at $\mathrm{Re}^* = 670$, a point within the instability region, a short distance from the lower branch of the neutral stability curve. In all three cases, flow travels into the unstable region therefore disturbances should become amplified at the downstream locations according to linear stability theory in section 4.2. The parameters used in all three simulation cases are listed in Table 4-4.

Case	1	2	3
Re^*	900	670	635
α^*	0.179250	0.229985	0.229985
β^*	0.059984	0.083770	0.084363
P	3	3	3
Δx	0.250	0.250	0.500
Δy	0.423	0.423	0.600
Δz	0.250	0.250	0.2500
Δt	0.010	0.010	0.020

Table 4-4. Case 1, 2 and 3 parameters

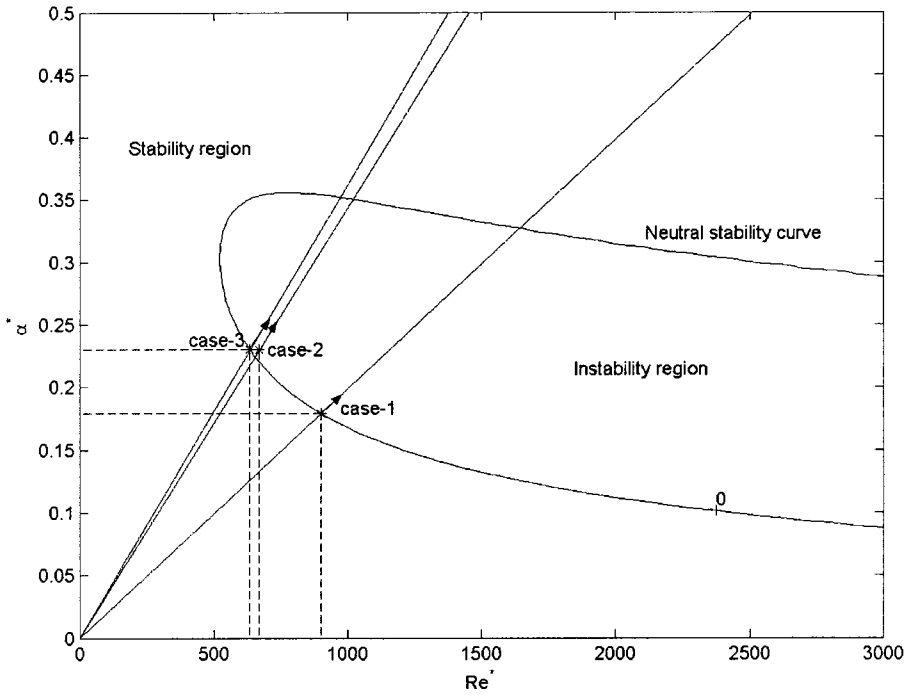

Figure 4-15. Cases 1, 2 and 3 on stability diagram of linear stability theory.

Case 1 –

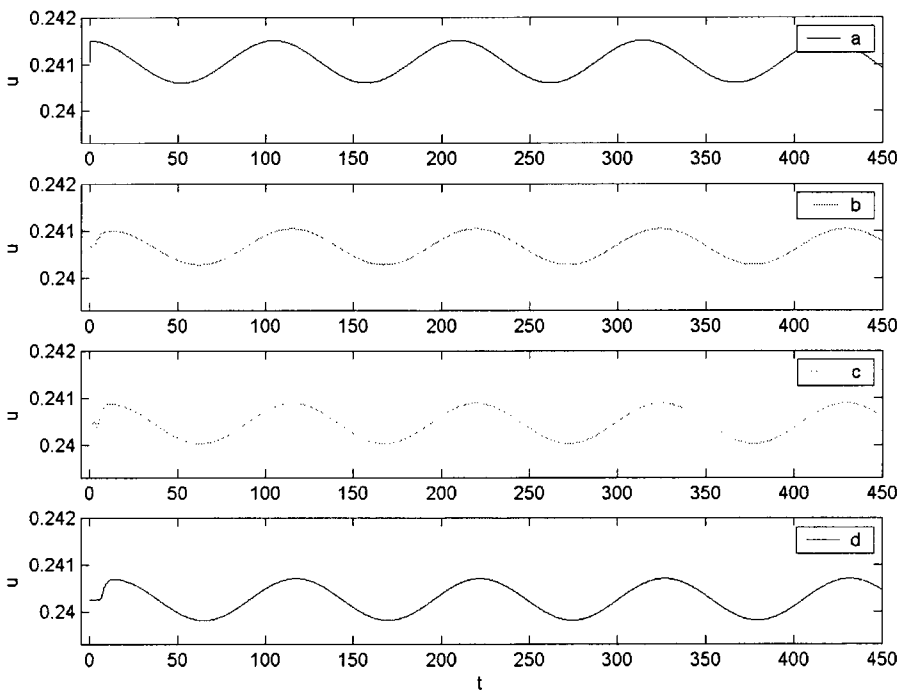

Figure 4-16. Temporal evolution plotted against u *and* t for case 1.

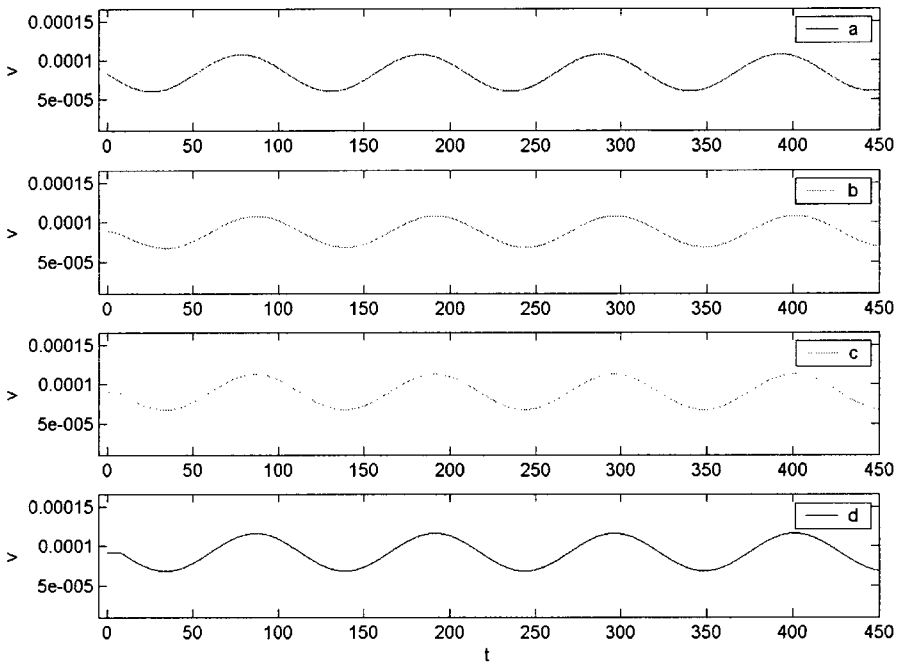

Figure 4-17. Temporal evolution plotted against v *and* t for case 1.

Case 2 -

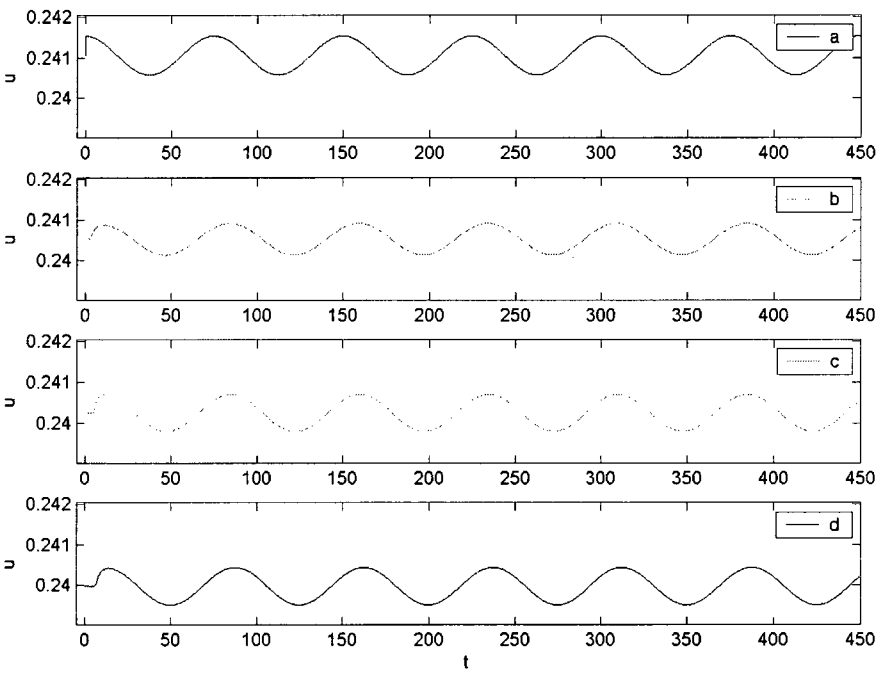

Figure 4-18. Temporal evolution plotted against u *and* t for case 2.

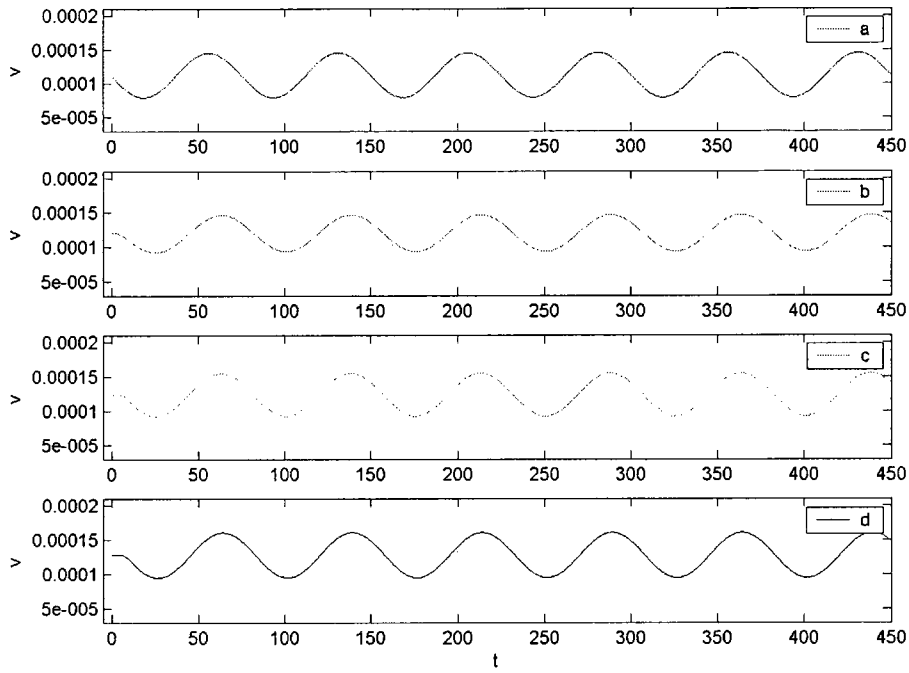

Figure 4-19. Temporal evolution plotted against v *and* t for case 2.

Case 3 -

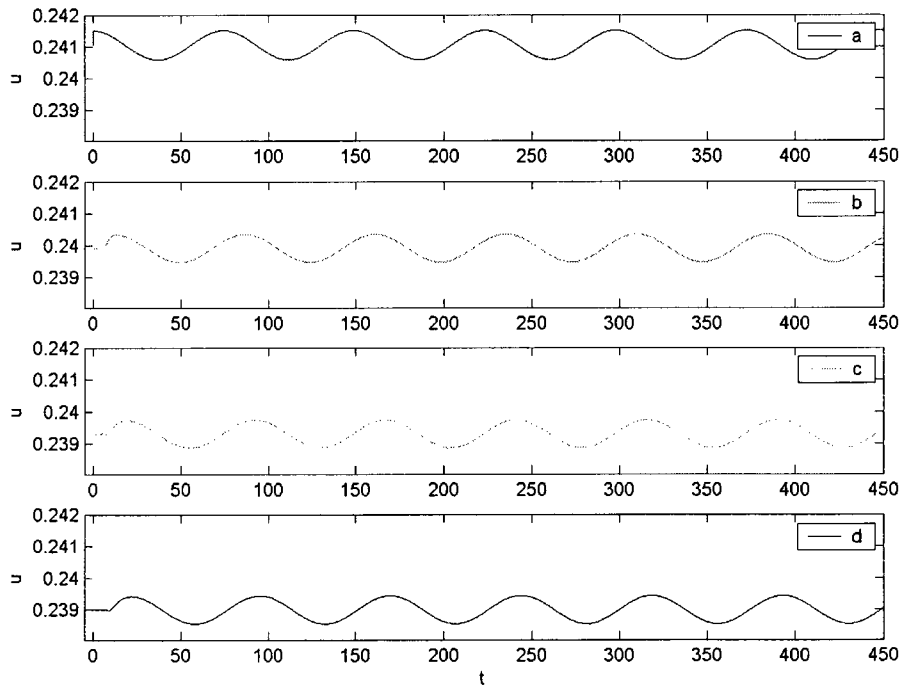

Figure 4-20. Temporal evolution plotted against u *and* t for case 3.

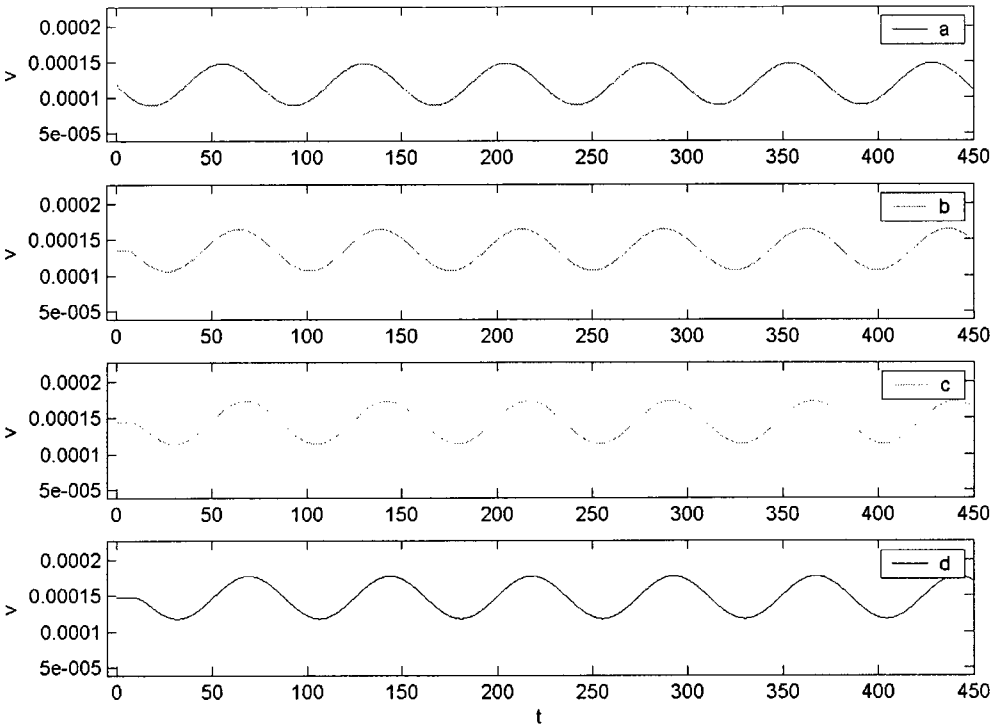

Figure 4-21. Temporal evolution plotted against v *and* t for case 3.

The Figure 4-16 through Figure 4-21 obtained for different Reynolds numbers again show that the temporal development of the flow and the propagation of the sinusoidal waves in the downstream direction as a result of the disturbances introduced at the inlet. From the observation of velocity distribution we can say that the time to reach periodic character increases proportionally as the flow travels in the downstream direction. At the downstream locations b, c and d, the amplitudes of the waves are tabulated in Table 4-5.

Location	Wave amplitudes					
	Case-1		Case - 2		Case -3	
Velocity	u x 10^{-3}	v x 10^{-4}	u x 10^{-3}	v x 10^{-4}	u x 10^{-3}	v x 10^{-4}
b	0.7697	0.3961	0.7852	0.5328	0.8743	0.5777
c	0.8609	0.4482	0.9016	0.6228	0.8799	0.5921
Outlet-d	0.8916	0.4768	0.9274	0.6568	0.8870	0.5937

Table 4-5.Wave amplitudes in the downstream locations for the cases 1, 2 and 3

In all three cases, amplitudes of the periodic oscillations continued to grow in the downstream direction as expected because the flow travels completely inside the unstable region. This fact justifies the statement that "the transition process is usually initiated by the amplification of unstable two dimensional waves through receptivity to the environmental disturbances [03]".

From the numerical results of case-1 and case-2, we noticed that the amplitudes of the waves are increasing with the increment of disturbance frequencies or wave number. After a certain disturbance frequency level, we cannot expect amplification in the downstream direction where the ray through the origin may not traverse the neutral stability curve. It means that the flow is in the fully stable region therefore transition behavior is hardly noticeable at all.

The case-3 ran with the similar disturbance parameters as the test case to check the reliability of the numerical results by varying grid parameters. The case-3 downstream locations are far from the locations considered for the test case. In both simulations, results show growth in wave amplitudes at downstream locations. This fact confirms the consistency of spectral element results for other grid sizes as well to investigate the initial stage of transition.

A remarkable observation all through the numerical experiments is the non-reflected velocity component waves at the outlet boundary. These results confirmed that the selected passive open boundary condition for the downstream boundary works better than any other alternative outflow boundary conditions in spectral element method.

Chapter 5

Conclusions and Future Work

An implicit time-marching, modal-spectral element discretization on a Gambit generated tetrahedral mesh was used due to its significant efficiency advantages over the other methods and provided a viable alternative to simulate our problem of interest with a relatively coarse grid. The ability of the code to run boundary layer problems was verified along the flat plate. This validation reproduced successfully the laminar Blasius solution over the full computational domain.

In the present analysis, the results of the numerical calculations demonstrated that the presented modal spectral element method for the solution of the complete Navier-Stokes equations was well suited for the investigation of initial stage of transition phenomena of incompressible boundary layer flows on a flat plate. For this prediction of pre-onset transition where integral quantities were of importance such as appropriate boundary and initial conditions and the linear stability theory is also likely to be a useful tool.

The more accurate treatment of boundary and initial conditions in the spectral element method led to observe the temporal evolution in the transitional region. The established boundary layer flow used periodic perturbation functions of small amplitudes from the linear stability theory to impress disturbances at the inflow. At the far-field, asymptotically decaying perturbation velocity boundary conditions were imposed to avoid erroneous disturbance arising due to the insufficient distance from the flat plate thus reducing the computational domain in the wall normal direction. Concerning the outflow boundary, passive open boundary condition was employed which allowed the

flow to leave the boundary without wave reflection. Due to the investigation of very small disturbances, a steady state solution of the Navier-Stokes equation was used as initial condition to eliminate the early distortions. These boundary and initial conditions predicted well the temporal development of the perturbations in the downstream direction. Finally this was compared with the test case calculations where the results gave in fairly close agreement with Fasel [05].

The conjecture is that this numerical method can now be applied with some confidence toward the investigation of some of the many still open questions concerning the growth of disturbances or larger disturbance amplitude interactions leading to laminar-turbulent transitional flows for which the linear stability theory is no longer valid to predict conditions. The present study is concerned with unbounded flow transition, although the related problems of bounded flows such as pipe and channel flows also may be solved in a similar manner.

The validated spectral element code would allow for future studies of more complex geometry and flow problems of interest efficiently such as the effects of surface roughness on laminar-turbulent transition process in shear layers by analyzing the stability of wavy-wall bounded shear flows [01] and the flows along an aero-foil with an angle of attack by considering curvilinear higher order tetrahedral elements on the non-linear boundaries with the priori knowledge of the preceding numerical effects. Further more, we could simulate the whole process of flow transition in three dimensional boundary layers including 2-D T-S waves, 3-D T-S waves, Λ shaped vortical structures, breakdown, turbulent spot formation and finally to fully turbulent flow with the help of three-dimensional disturbance environment.

The code could be extended further to perform large eddy simulation (LES) by incorporating a turbulence model such as dynamic Smagorinsky model, thus allowing us to solve for small scale phenomena within the available computational resources needed to obtain DNS solutions. Moreover, we can take the advantage of spectral element method on microfluidic systems to perform the fluid mixing, flow rectification and microscale cooling which are increasingly employing complex geometries.

Bibliography

[01] M.Asai, J.M.Floryan, "Experiments on the linear instability of flow in a wavy channel", European J.Mech., 25 (2006) 971-986

[02] G.A.Cardenas Casas, "Large Eddy Simulations Using Tetrahedral Finite Elements", M.A.Sc thesis, University of Toronto, 2003

[03] S.Deng, "Direct Numerical Simulation for flow transition over a flat plate", Ph.D. thesis, University of Texas at Arlington, 2005

[04] J.Dey, D.Das, "A note o the linear instability of the Blasius flow", Acta Mechanica 128 (1998) 253-258

[05] H.Fasel, "Investigation of the stability of boundary layers by a finite-difference model of the Navier-Stokes equations", J.Fluid. Mech., 78 (1976) 355-383

[06] H.Fasel, U.Rist, U.Konzelmann "Numerical Investigation of the Three-Dimensional Development in Boundary Layer Transition", AIAA paper No. 87-1203 (1987)

[07] H.Fasel and U.Konzelmann, "Non-parallel stability of a flat-plate boundary layer using the complete Navier-Stokes equations", J.Fluid. Mech.., 221 (1990) 311-347

[08] H.Fasel, "Untersuchungen zum Problem des Grenzschichtumschlages durch numerische Integration der Navier-Stokes Gleichungen", Dissertation, University of Stuttgart, 1974

[09] G.Fournier, F.Golanski, A.Pollard, "A novel outflow boundary condition for incompressible laminar wall-bounded flows", J.Comp.Phys., 227 (2008) 7077-7082

[10] M.Gaster, "A note on the relation between temporally increasing and spatially increasing disturbances in hydrodynamic stability", J.Fluid. Mech.14 (1962) 222-224

[11] M.Gaster, Prog. In Aero. Sci. 6 (1965) 2510

[12] P.M.Gresho, R.L.Sani, "Incompressible Flow and the Finite Element Method", John Wiley & Sons Ltd., 1999

[13] J.L Guermond, Jie Shen, "A new class of truly consistent splitting schemes for incompressible flows", J.Comp.Phys., 192 (2003) 262-276

[14] T.Hagstrom, "Conditions at the downstream boundary for simulations of viscous, incompressible flow", SIAM J.Sci.Stat.Comput.,12 (4): 843-858, 1991

[15] Q.He and X.P.Wang, "The effect of the boundary slip on the stability of shear flow",Wiley Inter Science, 88 (2008) 729-734

[16] T.Herbert, "Secondary instability of boundary layers", Annual review of fluid mechanics, 20-(1988) 487

[17] T.Herbert, "Onset of transition in boundary layers", Int. J. Numer. Meth. Fluids,8 (1988) 1151-1164

[18] J.Hoepffner, "Stability and control shear flows subject to stochastic excitations", KTH Stockholm, Ph.D. thesis, 2006

[19] A.P.Hooper, R.Grimshaw, "Two-dimensional disturbance growth of linear stable viscous shear flows", Phys.Fluids 8 (1996) 1424

[20] R.Jordinson, "The flat plate boundary layer. Part 1. Numerical integration of the Orr-Sommerfeld equation", J.Comp.Phys., 43 (1970) 801-811

[21] R.Jordinson, "The transition from laminar to turbulent flow over a flat plate space amplified, numerical solutions of the Orr-Sommerfeld equation", Ph.D. thesis, University of Edinburgh, 1968

[22] R.Joslin, C.Streett, C.Chang, "Validation of Three-Dimensional Incompressible Spatial Direct Numerical Simulation Code- A Comparison with Linear Stability and Parabolic Stability and Equation Theories for Boundary-Layer Transition on a Flat plate", NASA Technical Paper 3205

[23] R.E.Kaplan, ASRL-TR-116-1, Cambride Aeroelastic and Structures Lab.Rep., M.I.T. (STAR N-64-29052) 1964

[24] G.Karypis and V.Kumar, "Multilevel k-way Partitioning Scheme for Irregular Graphs", J.Parallel Distrib.Comput. 48(1), 96-129, 1998

[25] G.E.Karniadakis and S.J.Sherwin, "Spectral/hp Element Methods for CFD", Oxford University Press, Second Edition, 2005

[26] N.P.Kirchner, "Computational aspects of the spectral Galerkin FEM for the Orr-Sommerfeld equation", Int. J. Numer. Meth. Fluids, 32 (2000) 119-137

[27] P.Klebanoff, K.Tidstrom, and L.Sargent, "The three dimensional nature of boundary layer instability", J.Fluid Mech. 12-(1962)

[28] E.F.Kurtz, S.H.Crandall, "Computer-aided analysis of hydrodynamic stability, J.Math.Phys., 41 (1962) 264-279

[29] E.F.Kurtz, "A Study of the Stability of Laminar Parallel Flows", PhD thesis. M.I.T. (1961)

[30] T.Lee, "Newton's Divided Difference Interpolating Polynomials", 2001, http://www.cheric.org/ippage/e/ipdata/2001/13/node6.html

[31] C.Liu, Z.Liu, "Multigrid Direct Numerical Simulation of the whole process of Flow Transition in 3-D Boundary Layers", NASA Technical Memorandum, 1993

[32] P.P.Lynn, "Least squares finite element analysis of laminar boundary layer flows", Int. J. Numer. Meth. Eng, 8 (1974) 865-876

[33] F.A. Morrison, "Understanding Rheology", Oxford University Press, 2001

[34] R.Narasimha, J.Dey, "An extension of the Thwaites method for calculation of incompressible laminar boundary layers", J.Indina Inst.Sci. 70 (1990) 1-11

[35] M.J.Naughton, "On Numerical Boundary Conditions for the Navier-Stokes equations", Ph.D. thesis, California Institute of Technology, 1986

[36] C.Niewiadomski, "Spectral Element Solutions to flows in pipes with two planar curvatures", Ph.D. thesis, University of Toronto, 2007

[37] C.Niewiadomski, "Spectral Element Methods for the Stokes problem", MASc. thesis, University of Toronto, 2003

[38] C.Niewiadomski, M.Paraschivoiu, P.Sullivan "Equal order spectral element method solutions to flows in pipes with two planar curvatures", Int.J.Comp.Fluid Dynamics, 20 (2006) 287-292

[39] C.Niewiadomski, M.Paraschivoiu, P.Sullivan "A numerical study of fully developed laminar flows in pipes with two planar curvatures", Int. J. Numer. Meth. Fluids, 51 (2004) 849-879

[40] S.A.Orszag, "Accurate solution of the Orr-Sommerfeld stability equation", J.Fluid.Mech., 50 part 4 (1971) 689-703

[41] Orr,William M'F. "The Stability or Instability of the Steady Motions of a Perfect Liquid and of a Viscous Liquid. Part I.: A Perfect Liquid", Proc. Royal Irish Acad., Vol.27, Section A, No.2, 9-68, 1907

[42] Orr, William M'F., "The Stability or Instability of the Steady Motions of a Liquid. Part II.: A Viscous Liquid", Proc.Royal Irish Acad., Vol-27, Section A, No.3, 69-138, 1907

[43] M.R.Osborne, "Numerical methods for hydrodynamic stability problems", SIAM J. Appl. Math. 15 (1967) 539-557

[44] J.A. Ross, F.H.Barnes, J.C. Burns, M.A.Ross, "The flat plate boundary layer. Part 3. Comparison of theory with experiments", J.Fluid.Mech., 43 (1970) 819-832

[45] H.Schlichting, K.Gersten, "Boundary Layer Theory", 7th edition, New York, McGraw-Hill, 1979

[46] H.Schlichting, K.Gersten, "Boundary Layer Theory", Springer publication, 8th edition, 2000

[47] G.B. Schubauer, H.K. Skramstad, "Laminar-boundary layer oscillations and transition on a flat plate", NACA Report-909, 1948

[48] G.B. Schubauer, H.K. Skramstad, "Laminar-boundary layer oscillations and stability of laminar flow", J. Aeronaut. Sci., vol. 14, no. 2, 69-78, 1947

[49] S.F.Shen, "Calculated amplified oscillations in plane Poiseuille and Blasius flows", J.Aero.Soc. 21 (1954) 62

[50] S.J.Sherwin and G.E.Karniadakis, "Tetrahedral hp Finite Elements: Algorithms and Flow Simulations", J.of.Comp.Physics, 124 (1996) 14-45

[51] A.Sommerfeld, "Ein Beitrag zur Hydrodynamischen Erklaerung der Turbulenten Fluessigkeitsbewegungen", Congressio Int. dei Matimatica III, (1908) 116-124

[52] P.R.Spalart, "Direct simulation of a turbulent boundary layer up to $Re_\theta = 1410$, J.Comp.Phys., 187 (1988) 61-98

[53] C.L.Streett, M.G.Macaraeg, "Spectral Multi Domain for Large-Scale Fluid Dynamic Simulations", Int.J.Appl.Numer.Math., 6 (1989) 123-139

[54] J.T.Stuart, "Hydrodynamic stability", Appli.Mech.Rev., 18 (1965) 523-531

[55] R.Timman, J.A.Zaat, T.J.Burgerhout, Nat.Aero.Res.Inst.Amsterdam, N.L.L.Tech Note. F.193 (1956)

[56] W.Tollmien, "Uber die Entstehung der Turbulenz", Ges.d.Wiss.Gottingen, Math.Phys.Klasse,Nach., 21-44 (1929)

[57] W.Tollmien, (Dwight M.Miner, transl.), " The Production of Turbulence", NACA TM 609, 1931

[58] Wikipedia, "Orr-Sommerfeld equation", http://en.wikipedia.org

[59] J.A.C.Weideman and S.C.Reddy, "A MATLAB differentiation matrix suite", ACM Trans. Math. Software 26 (4),465-519 (1998, 2000)

[60] A.R.Wazzan, T.T.Okamura & A.M.O.Smith, "Spatial and temporal stability chats for the Falkner-Skan boundary layer profiles", McDonnell-Douglas Astronautics Co., Rep. no. DAC-67086 (1968)